Dislocation singularities in layered magneto-electro-elastic plates

Aurélien Vattré, E. Pan

Dislocation singularities in layered magneto-electro-elastic plates

A. Vattré[a,*], E. Pan[b]

[a]Onera, Université Paris-Saclay, Materials and Structures Department, 29 av. Division Leclerc, 92320 Châtillon, France
[b]College of Engineering and Institute of Pioneer Semiconductor Innovation, National Yang Ming Chiao Tung University, Taiwan

Abstract

A general and unified theory is formulated to investigate static and time-harmonic field solutions induced by dislocation loops and dislocation arrays in three-dimensional multilayered structures. Each homogeneous plate consists of an orthotropic magneto-electro-elastic material including nonlocal effects. While the nonlocal constitutive relations with multi-phase coupling are treated by means of the original Eringen model using a Helmholtz-type operator, the field expressions are based on the mathematically elegant and computationally powerful Stroh formalism in matrix form, consistently combined with double Fourier series expansions and the dual variable and position technique to propagate the extended solutions among the different layers of the multilayered systems. The time-harmonic dislocation loops are represented by a discontinuity in the prescribed elastic displacement, electric potential, and magnetic potential on arbitrarily-located rectangular and elliptical surfaces in the multilayered structures, while the dislocation arrays are composed of infinitely long, straight and uniformly spaced parallel dislocations with the same local Burgers vectors. The new field solutions are first validated against existing frameworks limited to static and local elasticity theory of these two types of extrinsic and intrinsic dislocations, and subsequently applied to analyze several unexplored effects on the dislocation-induced magneto-electro-elastic fields, namely the material anisotropy, interaction with internal heterophase interfaces, multi-phase coupling, nonlocal core-spreading parameter, finite-valued driving forces, vibration frequency, and stacking sequences. The numerical outcomes indicate that each effect is significant and neglecting any one of them lead to an erroneous prediction on the extrinsic and intrinsic dislocation-induced response, thus providing a suitable route for the design of advanced magneto-electro-elastic fabrication devices for energy harvesting applications.

Keywords: Anisotropic elasticity theory, dislocation loops and arrays, multilayered plates, multiferroics, nonlocal effects, time-harmonic field solutions

1. Introduction

Within the broad class of materials available today, multi-functional ferromagnetic and ferroelectric materials are widely used in a large range of intelligent and adaptative systems in aerospace, defense, automobile, medical, and electronic industries. In particular, a strong electromagnetic coupling effect can be realized by combining piezomagnetic and piezoelectric phases, thus providing the attractive ability of storing and converting different forms of energy among magnetic, electric and mechanical energies (vanSuchtelen, 1972, van den Boomgaard et al., 1974, van Run et al., 1974). In recent years, the opportunity to investigate novel components and device designs leads to an increasing amount of theoretical and numerical studies on the response and stability of magneto-electro-elastic (MEE) multilayered composites (Alshits et al., 1992, Harshe et al., 1993, Chung and Ting, 1995, Liu et al., 2001, Pan, 2001, 2002, Wang and Shen, 2002, Bichurin et al., 2003, Pan and Han, 2005, Challagulla and Georgiades, 2011, Zhang et al., 2017, Ghobadi et al., 2019, Ngak et al., 2019, Ren et al., 2020, Bustamante et al., 2021, Tang et al., 2021, Vinyas, 2021, Yu and Kang, 2021). Due to the beneficial cumulative effects and facile layer-by-layer fabrication processes, multilayered sequences with different faults are preferably arranged in plates. Because real MEE materials are, however, never perfectly manufactured, internal defects always exist, such as dislocation loops and dislocation arrays, which play a significant role in controlling the electromagnetic coupling performances (Nagarajan et al., 2005). An in-depth understanding of the influence of these imperfections on advanced self-sensing, self-diagnosing, self-adapting, and self-repairing properties, is also motivated by providing insights and predictions from general and fundamental frameworks dedicated to dislocated MEE heterostructures. The present work contributes to this current effort by introducing nonlocal and time-harmonic field solutions of dislocations in anisotropic multilayered and free-standing MEE plates in three dimensions, consistently obtained by use of the extended Stroh formalism combined with double Fourier series expansions.

In contrast to the considerable attention paid to the fundamental crack problems (Liu et al., 2001, Gao et al., 2003, Wang and Mai, 2003, Rao and Kuna, 2008, Li and Lee et al., 2010, Wan et al., 2013, Hu and Chen, 2015, Bagheri et al., 2015, Mousavi, 2015, Zhao et al., 2015, Bagheri et al., 2017, Zhao et al., 2019, Nourazar and Ayatollahi, 2020, Wu et al., 2021, Hsu and Hwu, 2022) as well the modeling of imperfectly bounded interfaces in MEE solids (Nan et al., 2003, Wang and Pan, 2007, Pan et al., 2009, Huang and Li, 2010, Espinosa et al., 2011, Kuo, 2013, Wang, 2015, Espinosa et al., 2017, Kuo et al., 2018, Jiang et al., 2019, Kuo et al., 2019, Pang et al., 2019, Yang and Li, 2019), the corresponding dislocation boundary-value problem has received little consideration in the literature for MEE bimaterials (Fang et al., 2005, Hao and Liu, 2006, Zheng et al., 2007, Han and Pan, 2013, Chu et al., 2013), and even less for free-standing MEE multilayers until recently (Moshtagh et al., 2019, Vattré

*Email address: aurelien.vattre@onera.fr

and Pan, 2019, Yuan et al., 2019). This circumstance is closely related to the difficulties in determining explicit expressions for the generalized MEE point-source Green's functions in inhomogeneous solids. In purely elastic media, localized dislocation loops and periodic dislocation arrays as well as their three-dimensional interactions are important topological defects with strong influences on the mechanical properties, such as ductility, hardness and yield strength (Bulatov and Cai, 2006, Kubin, 2013, Cai and Nix, 2016). In particular, dislocation networks are intrinsically part of grain boundaries, namely symmetric tilt and twist grain boundaries, as well as semicoherent heterophase interfaces between two adjoining solids, which in turn, can act as barriers to extrinsic dislocation motion (Hirth and Lothe, 1992) as well as sinks for point defects (Sutton and Balluffi, 1995, Vattré et al., 2016). The static dislocation-induced field solutions in anisotropic elastic materials (Eshelby et al., 1953, Stroh, 1958, 1962, Willis, 1970, Gavazza and Barnett, 1976, Ting, 1996, Wang, 1996, Ohsawa et al., 2009, Lazar and Kirchner, 2013, Pan, 2019), bimaterials (Pan, 2019, Chu and Pan, 2014, Wu et al., 2016, Vattré, 2017a,b, Vattré and Pan, 2018) and multimaterials (Vattré and Pan, 2019, Ghoniem and Han, 2005, Gao and Larson, 2015) have been extensively formulated, mainly within the framework of the classical continuum mechanics.

Nonlocal elasticity theories have been employed to determine adequately the non-singular dislocation field solutions by regularizing the standard singularities close to dislocation core regions (Vattré and Pan, 2019, Lazar and Agiasofitou, 2011, Lazar and Po, 2005, Lazar et al., 2020), which therefore leads univocally to the evaluation of the finite-valued driving forces on dislocations. In advanced topological crystalline insulators, lattice and misfit dislocations induce intriguing transport phenomena such as abnormal conductance and chiral magnetic effects (Ran et al., 2009, Tang and Fu, 2014, Sumiyoshi and Fujimoto, 2016, Chernodub and Zubkov, 2017, Hamasaki et al., 2017), which suggest a new route to optimizing MEE properties by controlling the extended field states in the vicinity of dislocations. These challenging applications necessitate the development of a unified three-dimensional MEE formalism to describe the different structural types of dislocation loops and dislocation arrays in multilayered anisotropic solids with multi-field MEE couplings. On the other hand, small-scale piezoelectric devices can be subjected to external excitations for energy harvesting purposes by means of vibration-to-electrical conversion mechanisms (Yang et al., 2017). In the quasi-static deformation regime, the long-range strain fields generated by the presence of dislocations lead to highly localized polarization gradients in nanoscale ferroelectric heterostructures (Nagarajan et al., 2005, Chu et al., 2004, Jia et al., 2009, Evans et al., 2021), while the corresponding role of dislocations on the time-harmonic stability of ferroelectric multilayers has not investigated yet, which therefore supports the proposed framework for free vibration responses of multilayered MEE composites.

In light of the above, the main objective is to self-consistently derive novel nonlocal and time-harmonic field solutions for dislocation loops and dislocation arrays in three-dimensional multilayered MEE systems. The unified approach is based on the mathematically elegant and computationally powerful Stroh formalism, combining further with the Fourier series transforms for dislocation loops and arrays in nonlocal MEE multilayers. Extended singularity-free field solutions for both types of dislocations are formulated in the context of the original nonlocal Eringen theory including a Helmholtz-type operator (Eringen, 2002). The time-harmonic dislocation loop is represented by a discontinuity in the elastic displacement, electric potential, and magnetic potential prescribed on rectangular or elliptical surfaces located arbitrarily in the multilayered structures, while the dislocation arrays are composed of infinitely long, straight and uniformly spaced parallel dislocations with the same characters. The stable and efficient implementation based on the dual variable and position procedure (Vattré and Pan, 2019, Pan, 2019, Liu et al., 2018) combined with the Stroh formalism is used to propagate the extended field solutions among different layers of the multilayered systems, in place of the standard transfer matrix method (Thomson, 1950) that can inevitably lead to numerical instabilities. The general and versatile framework can obviously be reduced to application problems of multiple dislocations in MEE full-space, half-space, bimaterial or layered half-space made of pure-elastic, piezoelectric or piezomagnetic solids.

This paper is outlined as follows. Section 2 describes the extended boundary-value problem of dislocation loops and dislocation arrays in MEE multilayers as well as the general time-harmonic solutions by means of double Fourier series expansion for each homogeneous and Eringen-type nonlocal plate. The recursive technique using the dual variable and position procedure is formulated in Section 3 by transferring multi-field matrices with respect to specific intrinsic boundary conditions for both types of dislocations. Section 4 deals with several application examples, especially the nonlocal MEE interaction between a dislocation loop and a dislocation network is investigated in a three-dimensional multiferroic $BaTiO_3$–$CoFe_2O_4$ composite structure.

2. Description and formulation of the extended boundary-value problem

Figure (1) illustrates the time-harmonic interaction between a dislocation loop and a dislocation array in the ideal three-dimensional MEE multilayered heterostructures, with parallel perfectly-bounded interfaces normal to $\boldsymbol{n} \parallel \boldsymbol{z} \parallel \boldsymbol{x}_3$. In a Cartesian coordinate system $(\boldsymbol{x},\boldsymbol{y},\boldsymbol{z}) = (\boldsymbol{x}_1,\boldsymbol{x}_2,\boldsymbol{x}_3)$, the complete system is composed of an arbitrary number of N-bonded orthotropic, dissimilar, nonlocal, and linearly MEE solids with perfectly connected internal interfaces, and the finite thickness for each λ^{th} plate is defined by $h_\lambda = z_\lambda - z_{\lambda-1}$ with $\lambda = 1,\ldots,N$. Both types of dislocations have their own extended characters, arbitrarily represented by a specific extended displacement jump at $z = z_L$ and $z = z_A$, respectively, including the intrinsic Burgers vectors. Futhermore, extended free-traction boundary conditions are assumed at the bottom and top surfaces, i.e. at $z = z_0 = 0$ and $z_N = H$, respectively, with H being the total thickness of the multilayers. In the following, summation over repeated Roman subscripts is implied, with the lowercase subscripts k running from 1 to 3, while the uppercase subscripts K from 1 to 5.

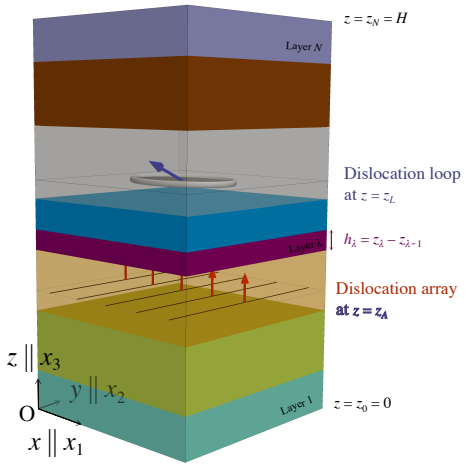

Figure 1: Time-harmonic interaction between a dislocation loop and a dislocation array embedded in a three-dimensional multilayered magneto-electro-elastic heterostructure. The multilayer is described in the global and fixed Cartesian coordinate system $(\mathrm{O}, x \parallel x_1, y \parallel x_2, z \parallel x_3)$, and is composed of N-bonded orthotropic, dissimilar, nonlocal, and magneto-electro-elastic plates with perfectly connected internal interfaces. Without loss of generality, extended free-traction boundary conditions are assumed at the bottom and top surfaces, i.e. at $z = z_0$ and z_N, respectively, while the extended displacement jumps for the dislocation loop and array, including their intrinsic Burgers vectors, are arbitrarily defined at $z = z_L$ and $z = z_A$, respectively.

2.1. Nonlocal constitutive and governing equations

For each linear and homogeneous Eringen nonlocal plate, the extended displacement field u_K is defined by

$$u_K = \begin{cases} u_k & K = k = 1,2,3 \\ \phi & K = 4 \\ \psi & K = 5\,, \end{cases} \tag{1}$$

where u_k, ϕ, and ψ are the standard elastic displacement (in m), the electric potential (in V), and the magnetic potential (in A), respectively. The extended strain γ_{Kj} is given by

$$\gamma_{Kj} = \begin{cases} \gamma_{kj} = \frac{1}{2}\left(u_{k,j} + u_{j,k}\right) & K = k = 1,2,3 \\ E_j = -\phi_{,j} & K = 4 \\ H_j = -\psi_{,j} & K = 5\,, \end{cases} \tag{2}$$

for which the comma followed by lowercase subscript k denotes partial differentiation with respect to the position x_k, while γ_{kj} is the elastic strain (dimensionless), E_j is the electric field (in $\mathrm{V/m}$), H_j is the magnetic field (in $\mathrm{A/m}$). On the other hand, the the extended stress field σ_{iJ} is defined by

$$\sigma_{kJ} = \begin{cases} \sigma_{kj} & J = j = 1,2,3 \\ D_k & J = 4 \\ B_k & J = 5\,, \end{cases} \tag{3}$$

with σ_{kj} the components of the elastic stress (in $\mathrm{N/m^2}$), D_k the electric displacement (in $\mathrm{C/m^2}$), and B_k the magnetic induction (in $\mathrm{N/A.m}$), and the extended traction vector is therefore given by

$$t_J = \sigma_{kJ}\, n_k\,, \tag{4}$$

with normal n_k. For time-harmonic deformation state with the given frequency of excitation ω in rad/s, and without body forces, thermal effects, electric current densities, electric and magnetic charge densities, the governing partial differential equation of vibration motion and the extended constitutive relations for each Eringen nonlocal plate read

$$\sigma_{iJ,i} + \rho\omega^2 \delta_{jJ}\, u_J = 0\,, \tag{5a}$$

$$\left(1 - l_E^2 \nabla^2\right) \sigma_{iJ} = c_{iJKl}\, \gamma_{Kl}\,, \tag{5b}$$

where ρ is the mass density (in $\mathrm{kg/m^3}$), l_E is the nonlocal parameter (in m), ∇^2 is the three-dimensional Laplacian operator, and the extended stiffness tensor is defined for each orthotropic MEE layer by

$$c_{iJKl} = \begin{cases} c_{ijkl} & J, K = j, k = 1,2,3 \\ e_{lij} & J = j = 1,2,3,\ K = 4 \\ e_{ikl} & J = 4,\ K = k = 1,2,3 \\ q_{lij} & J = j = 1,2,3,\ K = 5 \\ q_{ikl} & J = 5,\ K = k = 1,2,3 \\ -\alpha_{il} & J = 4,\ K = 5,\ \text{or},\ \ K = 4,\ J = 5 \\ -\epsilon_{il} & J, K = 4 \\ -\mu_{il} & J, K = 5\,, \end{cases} \tag{6}$$

where c_{ijlm}, e_{kij}, q_{kij}, α_{ij}, ϵ_{il}, μ_{il} are the elastic moduli (in N/m^2), piezoelectric (in C/m^2), piezomagnetic (in N/A.m), magnetoelectric (in C/A.m), dielectric permittivity (in C^2/N.m^2) and magnetic permeability (in N.s^2/C^2) coefficients, respectively, which satisfy the following symmetries: $c_{ijlm} = c_{jilm} = c_{ijml} = c_{lmij}$, $e_{kij} = e_{kji}$, $q_{kij} = q_{kji}$, $\alpha_{ij} = \alpha_{ji}$, $\epsilon_{ij} = \epsilon_{ji}$, and $\mu_{ij} = \mu_{ji}$. In terms of the extended displacements, eqs. (5) are rewritten as follows

$$-\left(1 - l_E^2 \nabla^2\right) \rho \omega^2 \delta_{jJ}\, u_J = c_{iJKl}\, u_{K,li}\,, \tag{7}$$

which becomes the main time-harmonic differential equation to be solved. To distinguish the general field solution for each plate from the global solution for the multilayered systems, a convenient local coordinate system (x_1, x_2, z') is attached to the individual λ^{th} layer, with origin at the point where the global $x_3 \parallel z$ axis intersects the bottom interface of the λ^{th} plate. In the local Cartesian coordinate system, the five-dimensional field solution of the extended displacement vector u_K in eq. (7) is sought in the complex standard form and is expressed as a product of a function of position and a separate function of time, as follows

$$u_K = \mathrm{e}^{i\omega t}\, \hat{u}_K(x_1, x_2, z')\,, \tag{8}$$

where the time-independent nonlocal displacement vector $\hat{u}_K$ is expressed using the two-dimensional Fourier series expansion ansatz (Srinivas and Rao, 1970, Dobyns, 1981), as follows

$$u_K = \begin{bmatrix} u_1 \\ u_2 \\ u_3 \\ \phi \\ \psi \end{bmatrix} = \mathrm{e}^{i\omega t} \sum_{m=1}^{\infty} \sum_{n=1}^{\infty} \begin{bmatrix} \bar{u}_1(z') \cos(p_m x_1) \sin(q_n x_2) \\ \bar{u}_2(z') \sin(p_m x_1) \cos(q_n x_2) \\ \bar{u}_3(z') \sin(p_m x_1) \sin(q_n x_2) \\ \bar{\phi}(z') \sin(p_m x_1) \sin(q_n x_2) \\ \bar{\psi}(z') \sin(p_m x_1) \sin(q_n x_2) \end{bmatrix} = \mathrm{e}^{i\omega t} \sum_{m=1}^{\infty} \sum_{n=1}^{\infty} \mathrm{e}^{sz'} \begin{bmatrix} a_1 \cos(p_m x_1) \sin(q_n x_2) \\ a_2 \sin(p_m x_1) \cos(q_n x_2) \\ a_3 \sin(p_m x_1) \sin(q_n x_2) \\ a_4 \sin(p_m x_1) \sin(q_n x_2) \\ a_5 \sin(p_m x_1) \sin(q_n x_2) \end{bmatrix}, \tag{9}$$

where the half-wave numbers are given by $p_m = m\pi/L_x$ and $q_n = n\pi/L_y$, with m and n being two positive integers, and L_x and L_y the dimensions in the $x \parallel x_1$- and $y \parallel x_2$- directions of the multilayered structures. The extended traction vector t_K is also written as

$$t_K = \begin{bmatrix} \sigma_{31} \\ \sigma_{32} \\ \sigma_{33} \\ D_3 \\ B_3 \end{bmatrix} = \mathrm{e}^{i\omega t} \sum_{m=1}^{\infty} \sum_{n=1}^{\infty} \begin{bmatrix} \bar{\sigma}_{31}(z') \cos(p_m x_1) \sin(q_n x_2) \\ \bar{\sigma}_{32}(z') \sin(p_m x_1) \cos(q_n x_2) \\ \bar{\sigma}_{33}(z') \sin(p_m x_1) \sin(q_n x_2) \\ \bar{D}_3(z') \sin(p_m x_1) \sin(q_n x_2) \\ \bar{B}_3(z') \sin(p_m x_1) \sin(q_n x_2) \end{bmatrix} = \mathrm{e}^{i\omega t} \sum_{m=1}^{\infty} \sum_{n=1}^{\infty} \mathrm{e}^{sz'} \begin{bmatrix} b_1 \cos(p_m x_1) \sin(q_n x_2) \\ b_2 \sin(p_m x_1) \cos(q_n x_2) \\ b_3 \sin(p_m x_1) \sin(q_n x_2) \\ b_4 \sin(p_m x_1) \sin(q_n x_2) \\ b_5 \sin(p_m x_1) \sin(q_n x_2) \end{bmatrix}, \tag{10}$$

where both superscripts over p_m and q_n are omitted to avoid notational complexity, unless stipulated. Both vectors a_K and b_K in eqs. (9) and (10) are written as follows

$$\begin{aligned} \boldsymbol{a} &= \left[a_1, a_2, a_3, a_4, a_5\right]^{\mathrm{t}} \\ \boldsymbol{b} &= \left[b_1, b_2, b_3, b_4, b_5\right]^{\mathrm{t}}, \end{aligned} \tag{11}$$

respectively, for which nonlocal relations between the expansion coefficients of the displacement and traction vectors can be derived by substituting eqs. (9) and (10) into the constitutive eq. (5b), such that

$$\left(1 - l_E^2\left(s^2 - p^2 - q^2\right)\right) \boldsymbol{b} = \left[-\mathbf{R}^{\mathrm{t}} + s\mathbf{T}\right] \boldsymbol{a} = -s^{-1} \left[\mathbf{Q} + \rho\omega^2 \left(1 - l_E^2\left(s^2 - p^2 - q^2\right)\right) \mathbf{I}_{5\times5} + s\mathbf{R}\right] \boldsymbol{a}\,, \tag{12}$$

where the three involved 5×5 matrices $\mathbf{R}$, $\mathbf{T}$ and $\mathbf{Q}$ are given by

$$\mathbf{R} = \begin{bmatrix} 0 & 0 & pc_{13} & pe_{31} & pq_{31} \\ 0 & 0 & qc_{23} & qe_{32} & qq_{32} \\ -pc_{55} & -qc_{44} & 0 & 0 & 0 \\ -pe_{15} & -qe_{24} & 0 & 0 & 0 \\ -pq_{15} & -qq_{24} & 0 & 0 & 0 \end{bmatrix}, \tag{13a}$$

$$\mathbf{T} = \begin{bmatrix} c_{55} & 0 & 0 & 0 & 0 \\ & c_{44} & 0 & 0 & 0 \\ & & c_{33} & e_{33} & q_{33} \\ & \text{sym} & & -\epsilon_{33} & -\alpha_{33} \\ & & & & -\mu_{33} \end{bmatrix} = \mathbf{T}^{\mathrm{t}}, \tag{13b}$$

$$\mathbf{Q} = -\begin{bmatrix} p^2c_{11} + q^2c_{66} & pq(c_{12} + c_{66}) & 0 & 0 & 0 \\ & p^2c_{66} + q^2c_{22} & 0 & 0 & 0 \\ & & p^2c_{55} + q^2c_{44} & p^2e_{15} + q^2e_{24} & p^2q_{15} + q^2q_{24} \\ & \text{sym} & & -p^2\epsilon_{11} - q^2\epsilon_{22} & -p^2\alpha_{11} - q^2\alpha_{22} \\ & & & & -p^2\mu_{11} - q^2\mu_{22} \end{bmatrix} = \mathbf{Q}^{\mathrm{t}}, \tag{13c}$$

while $\mathbf{I}_{5\times5}$ is the identity matrix. Furthermore, substituting eqs. (9) and (10) into the constitutive eq. (7) lead to a quadratic eigenequation, as follows

$$\left[\mathbf{Q} + \rho\omega^2 \left(1 + l_E^2\left(p^2 + q^2\right)\right) \mathbf{I}_{5\times5} + s\left(\mathbf{R} - \mathbf{R}^{\mathrm{t}}\right) + s^2\left(\mathbf{T} - \rho\omega^2 l_E^2 \mathbf{I}_{5\times5}\right)\right] \boldsymbol{a} = \mathbf{0}\,, \tag{14}$$

which, combined with eq. (12), can be recast by the following linear eigensystem of equations, i.e.

$$\begin{bmatrix} \widetilde{\mathbf{T}}^{-1}\mathbf{R}^{\mathrm{t}} & \widetilde{\mathbf{T}}^{-1} \\ -\widetilde{\mathbf{Q}}-\mathbf{R}\widetilde{\mathbf{T}}^{-1}\mathbf{R}^{\mathrm{t}} & -\mathbf{R}\widetilde{\mathbf{T}}^{-\mathrm{t}} \end{bmatrix} \begin{bmatrix} \boldsymbol{a} \\ \boldsymbol{d} \end{bmatrix} = s \begin{bmatrix} \boldsymbol{a} \\ \boldsymbol{d} \end{bmatrix} \tag{15}$$

where the 5×5 time-harmonic $\widetilde{\mathbf{T}}$ and $\widetilde{\mathbf{Q}}$ matrices are given by

$$\widetilde{\mathbf{Q}} = \mathbf{Q} + \rho\omega^2\left(1 + l_E^2\left(p^2+q^2\right)\right)\mathbf{I}_{5\times 5} = \widetilde{\mathbf{Q}}^{\mathrm{t}}, \tag{16a}$$

$$\widetilde{\mathbf{T}} = \mathbf{T} - \rho\omega^2 l_E^2\,\mathbf{I}_{5\times 5} = \widetilde{\mathbf{T}}^{\mathrm{t}}, \tag{16b}$$

while the 5×1 constant column matrix $\boldsymbol{d}$ is defined by

$$\boldsymbol{d} = \left[-\mathbf{R}^{\mathrm{t}} + s\left(\mathbf{T} - \rho\omega^2 l_E^2\mathbf{I}_{5\times 5}\right)\right]\boldsymbol{a} = -s^{-1}\left[\mathbf{Q} + \rho\omega^2\left(1 + l_E^2\left(p^2+q^2\right)\right)\mathbf{I}_{5\times 5} + s\mathbf{R}\right]\boldsymbol{a}, \tag{17}$$

with respect to $\mathbf{R}$, $\mathbf{T}$ and $\mathbf{Q}$ from eqs. (13).

2.2. General displacement and stress field solutions for each homogeneous plate

The eigenequation (15) is the extended Stroh sextic formalism that provides a general solution for the time-harmonic deformation state in each linear anisotropic plate, within which the eigenvalues s and eigenvectors $\boldsymbol{a}$ depend on ω, l_E, m, and n, as well as the material properties listed in eq. (6). These complex eigenvalues are conveniently arranged such that $\mathrm{Re}\,s_1 \geq \ldots \geq \mathrm{Re}\,s_{10}$, and $p_{K+5} = p_K^*$, where the asterisk indicates complex conjugates of solutions, due to the positive definiteness of the magnetic, electric, and elastic strain energy densities. Without the proportional sine and cosine terms as well as the time-dependent factor $\mathrm{e}^{i\omega t}$ in eqs. (9) and (10) for clarity, the general z'-dependent displacement and traction solutions in the Fourier-transformed domain can be expressed in terms of the Stroh formalism in any given layer λ bonded by the lower and upper interfaces at $z_{\lambda-1}$ and z_λ, respectively, as follows

$$\begin{bmatrix} \bar{\boldsymbol{u}}(z') \\ \bar{\boldsymbol{t}}(z') \end{bmatrix} = \begin{bmatrix} \mathbf{A}_\dagger & \mathbf{A}_{\dagger\dagger} \\ \mathbf{B}_\dagger & \mathbf{B}_{\dagger\dagger} \end{bmatrix} \begin{bmatrix} \left\langle \mathrm{e}^{\boldsymbol{s}_\dagger(z-z_\lambda)} \right\rangle & \mathbf{0}_{5\times 5} \\ \mathbf{0}_{5\times 5} & \left\langle \mathrm{e}^{\boldsymbol{s}_{\dagger\dagger}(z-z_{\lambda-1})} \right\rangle \end{bmatrix} \begin{bmatrix} \mathbf{K}_\dagger \\ \mathbf{K}_{\dagger\dagger} \end{bmatrix}, \tag{18}$$

with $\mathbf{A}_\dagger$ and $\mathbf{A}_{\dagger\dagger}$ being the primary eigenvector matrices defined by

$$\mathbf{A}_\dagger = \left[\boldsymbol{a}_1, \boldsymbol{a}_2, \boldsymbol{a}_3, \boldsymbol{a}_4, \boldsymbol{a}_5\right], \quad \mathbf{A}_{\dagger\dagger} = \left[\boldsymbol{a}_6, \boldsymbol{a}_7, \boldsymbol{a}_8, \boldsymbol{a}_9, \boldsymbol{a}_{10}\right], \tag{19}$$

while the elements $\boldsymbol{b}_K$ of secondary eigenvector matrices $\mathbf{B}_\dagger = [\boldsymbol{b}_1, \boldsymbol{b}_2, \boldsymbol{b}_3, \boldsymbol{b}_4, \boldsymbol{b}_5]$ and $\mathbf{B}_{\dagger\dagger} = [\boldsymbol{b}_6, \boldsymbol{b}_7, \boldsymbol{b}_8, \boldsymbol{b}_9, \boldsymbol{b}_{10}]$ are deduced from $\boldsymbol{a}_K$, as follows

$$\boldsymbol{b}_K = \left(1 - l_E^2(s_K^2 - p^2 - q^2)\right)^{-1}\left[-\mathbf{R}^{\mathrm{t}} + s_K\mathbf{T}\right]\boldsymbol{a}_K = \left(1 - l_E^2(s_K^2 - p^2 - q^2)\right)^{-1}\left(\boldsymbol{d}_K + \rho\omega^2 l_E^2\, s_K\,\mathbf{I}_{5\times 5}\boldsymbol{a}_K\right), \tag{20}$$

by virtue of eq. (17). Both matrices $\mathbf{A}_\dagger$ and $\mathbf{B}_\dagger$ are also the collections of eigenvectors associated with the first five eigenvalues $\boldsymbol{s}_\dagger$, while $\mathbf{A}_{\dagger\dagger}$ and $\mathbf{B}_{\dagger\dagger}$ are related to the eigenvectors of the eigenvalues $\boldsymbol{s}_{\dagger\dagger}$, given by

$$\boldsymbol{s}_\dagger = \left[s_1, s_2, s_3, s_4, s_5\right]^{\mathrm{t}}, \quad \boldsymbol{s}_{\dagger\dagger} = \left[s_6, s_7, s_8, s_9, s_{10}\right]^{\mathrm{t}}, \tag{21}$$

which are defined in the z'-dependent diagonal and exponential matrices in eq. (18), as follows

$$\left\langle \mathrm{e}^{\boldsymbol{s}_\dagger z'} \right\rangle = \mathrm{diag}\left[\mathrm{e}^{s_1 z'}, \mathrm{e}^{s_2 z'}, \mathrm{e}^{s_3 z'}, \mathrm{e}^{s_4 z'}, \mathrm{e}^{s_5 z'}\right], \quad \left\langle \mathrm{e}^{\boldsymbol{s}_{\dagger\dagger} z'} \right\rangle = \mathrm{diag}\left[\mathrm{e}^{s_6 z'}, \mathrm{e}^{s_7 z'}, \mathrm{e}^{s_8 z'}, \mathrm{e}^{s_9 z'}, \mathrm{e}^{s_{10} z'}\right], \tag{22}$$

while $\boldsymbol{K}_\dagger$ and $\boldsymbol{K}_{\dagger\dagger}$ are 5×1 constant column matrices to be determined from the internal and external boundary conditions. For each pair of integers m and n, the general solutions of eqs. (9) and (10) for the extended displacement and traction field vectors in each homogenous nonlocal plate are also obtained at any material point and any time in each plate by introducing the sine and cosine terms as well as the time-dependent factor $\mathrm{e}^{i\omega t}$ in eq. (18) and by solving the eigensystem in eq. (15) based on the extended Stroh formalism. Furthermore, the remaining in-plane stresses τ_K are organized as follows

$$\tau_K = \begin{bmatrix} \sigma_{11} \\ \sigma_{12} \\ \sigma_{22} \\ D_1 \\ D_2 \\ B_1 \\ B_2 \end{bmatrix} = \mathrm{e}^{i\omega t}\sum_{m=1}^{\infty}\sum_{n=1}^{\infty}\mathrm{e}^{sz'} \begin{bmatrix} c_1\sin(p_m x_1)\sin(q_n x_2) \\ c_2\cos(p_m x_1)\cos(q_n x_2) \\ c_3\sin(p_m x_1)\sin(q_n x_2) \\ c_4\cos(p_m x_1)\sin(q_n x_2) \\ c_5\sin(p_m x_1)\cos(q_n x_2) \\ c_6\cos(p_m x_1)\sin(q_n x_2) \\ c_7\sin(p_m x_1)\cos(q_n x_2) \end{bmatrix}, \tag{23}$$

within which the coefficient c_M, with $M = 1,\ldots,7$, are related to a_K by

$$\begin{bmatrix} c_1 \\ c_2 \\ c_3 \\ c_4 \\ c_5 \\ c_6 \\ c_7 \end{bmatrix} = \left(1 - l_E^2(s^2 - p^2 - q^2)\right)^{-1} \begin{bmatrix} -pc_{11} & -qc_{12} & sc_{13} & se_{31} & sq_{31} \\ qc_{66} & pc_{66} & 0 & 0 & 0 \\ -pc_{12} & -qc_{22} & sc_{23} & se_{32} & sq_{32} \\ se_{15} & 0 & pe_{15} & -p\epsilon_{11} & -p\alpha_{11} \\ 0 & se_{24} & qe_{24} & -q\epsilon_{22} & -q\alpha_{22} \\ -sq_{15} & 0 & pq_{15} & -p\alpha_{11} & -p\mu_{11} \\ 0 & sq_{24} & qq_{24} & -q\alpha_{22} & -q\mu_{22} \end{bmatrix} \begin{bmatrix} a_1 \\ a_2 \\ a_3 \\ a_4 \\ a_5 \end{bmatrix}, \tag{24}$$

which is obtained by substituting the displacement expansion eq. (9) and the in-plane stress eq. (23) into eq. (5b).

3. Nonlocal and time-harmonic recursive field solutions in MEE multilayered systems

Instead of using higher-order finite element ressources for multilayered plates, various semi-analytical layered matrix methods have been proposed in the literature, as reviewed by Pan (2019), such as the transfer matrix method (Thomson, 1950, Haskell, 1953, Singh, 1970, Pan, 1989), the delta matrix method (Castaings and Hosten, 1993, Hosten and Castaings, 1993), the stiffness matrix method (Nayfeh, 1991, Wang and Rokhlin, 2001, Rokhlin and Wang, 2002), the hybrid compliance-stiffness matrix method (Tan, 2006, 2007, 2011), the reverberation ray matrix method (Yuan et al., 2019, Howard and Pao, 1998, Su et al., 2002, Pao et al., 2007), the precise integration method (Zhong, 2004, Gao et al., 2013, Ai and Cheng, 2014). While the standard transfer matrix method leads numerical instability at high frequency-thickness products, the latter precise integration method has inspired the recent dual variable and position technique (Vattré and Pan, 2019, Pan, 2019, Liu et al., 2018) for the present nonlocal and time-harmonic field solutions for dislocations in multilayered structures, which is unconditionally stable with high accuracy (Vattré and Pan, 2019, Pan, 2019, Zhou et al., 2019). The technique is also used to propagate the Fourier expansion solutions among different layers from the bottom to the upper free surfaces, through the different types of dislocations.

3.1. Recursive field relations using the dual variable and position technique

In the context of the dual variable and position technique in the Fourier-transformed domain, the location z' is substituted by $z'_{\lambda-1}$ into the linear system in eq. (18), so that the general solutions in terms of displacements and tractions lead to

$$\begin{bmatrix} \bar{\boldsymbol{u}}\left(z'_{\lambda-1}\right) \\ \bar{\boldsymbol{t}}\left(z'_{\lambda-1}\right) \end{bmatrix} = \begin{bmatrix} \mathbf{A}_{\dagger} & \mathbf{A}_{\dagger\dagger} \\ \mathbf{B}_{\dagger} & \mathbf{B}_{\dagger\dagger} \end{bmatrix} \begin{bmatrix} \left\langle \mathrm{e}^{\boldsymbol{s}_{\dagger} h_{\lambda}} \right\rangle & \mathbf{0}_{5\times5} \\ \mathbf{0}_{5\times5} & \mathbf{I}_{5\times5} \end{bmatrix} \begin{bmatrix} \mathbf{K}_{\dagger} \\ \mathbf{K}_{\dagger\dagger} \end{bmatrix}, \tag{25}$$

while similarly substituting z'_{λ} into eq. (18), and combining the resultant relation with eq. (25), both unknown complex vectors $\mathbf{K}_{\dagger}$ and $\mathbf{K}_{\dagger\dagger}$ can be removed to meet cross relations between field solutions at $z' = z'_{\lambda-1}$ and $z' = z'_{\lambda}$, as follows

$$\begin{bmatrix} \bar{\boldsymbol{u}}\left(z'_{\lambda-1}\right) \\ \bar{\boldsymbol{t}}\left(z'_{\lambda}\right) \end{bmatrix} = \begin{bmatrix} \mathbf{S}_{11}^{\lambda} & \mathbf{S}_{12}^{\lambda} \\ \mathbf{S}_{21}^{\lambda} & \mathbf{S}_{22}^{\lambda} \end{bmatrix} \begin{bmatrix} \bar{\boldsymbol{u}}\left(z'_{\lambda}\right) \\ \bar{\boldsymbol{t}}\left(z'_{\lambda-1}\right) \end{bmatrix} = \begin{bmatrix} \mathbf{A}_{\dagger}\left\langle \mathrm{e}^{-\boldsymbol{s}_{\dagger} h_{\lambda}} \right\rangle & \mathbf{A}_{\dagger\dagger} \\ \mathbf{B}_{\dagger} & \mathbf{B}_{\dagger\dagger}\left\langle \mathrm{e}^{\boldsymbol{s}_{\dagger\dagger} h_{\lambda}} \right\rangle \end{bmatrix} \begin{bmatrix} \mathbf{A}_{\dagger} & \mathbf{A}_{\dagger\dagger}\left\langle \mathrm{e}^{\boldsymbol{s}_{\dagger\dagger} h_{\lambda}} \right\rangle \\ \mathbf{B}_{\dagger}\left\langle \mathrm{e}^{-\boldsymbol{s}_{\dagger} h_{\lambda}} \right\rangle & \mathbf{B}_{\dagger\dagger} \end{bmatrix}^{-1} \begin{bmatrix} \bar{\boldsymbol{u}}\left(z'_{\lambda}\right) \\ \bar{\boldsymbol{t}}\left(z'_{\lambda-1}\right) \end{bmatrix}, \tag{26}$$

where the 2×2 five-dimensional block matrices contains real-valued elements. Furthermore, the propagation relations of the expansion coefficient solutions at both interfaces z_{λ} and $z_{\lambda+1}$ for the upper adjacent layer are similarly defined by

$$\begin{bmatrix} \bar{\boldsymbol{u}}\left(z'_{\lambda}\right) \\ \bar{\boldsymbol{t}}\left(z'_{\lambda+1}\right) \end{bmatrix} = \begin{bmatrix} \mathbf{S}_{11}^{\lambda+1} & \mathbf{S}_{12}^{\lambda+1} \\ \mathbf{S}_{21}^{\lambda+1} & \mathbf{S}_{22}^{\lambda+1} \end{bmatrix} \begin{bmatrix} \bar{\boldsymbol{u}}\left(z'_{\lambda+1}\right) \\ \bar{\boldsymbol{t}}\left(z'_{\lambda}\right) \end{bmatrix}, \tag{27}$$

for which the in-built elements are written in terms of the corresponding Stroh eigensolutions to the plate $\lambda+1$ and thickness $h_{\lambda+1}$. Because the internal interface at z_{λ} between both adjacent λ and $\lambda+1$ layers is perfectly bonded, the Fourier-transformed displacement and traction vectors at $z = z_{\lambda}$ are continuous, which leads to important recursive relations between interfaces $z_{\lambda-1}$ and $z_{\lambda+1}$ by combining eqs. (26) and (27) together, as follows

$$\begin{bmatrix} \bar{\boldsymbol{u}}\left(z'_{\lambda-1}\right) \\ \bar{\boldsymbol{t}}\left(z'_{\lambda+1}\right) \end{bmatrix} = \begin{bmatrix} \mathbf{S}_{11}^{\lambda:\lambda+1} & \mathbf{S}_{12}^{\lambda:\lambda+1} \\ \mathbf{S}_{21}^{\lambda:\lambda+1} & \mathbf{S}_{22}^{\lambda:\lambda+1} \end{bmatrix} \begin{bmatrix} \bar{\boldsymbol{u}}\left(z'_{\lambda+1}\right) \\ \bar{\boldsymbol{t}}\left(z'_{\lambda-1}\right) \end{bmatrix}, \tag{28}$$

where the superscript $^{\lambda:\lambda+1}$ means the resulting propagation matrix from layer λ to layer $\lambda+1$, and the five-dimensional layer-to-layer submatrices are expressed as

$$\begin{cases} \mathbf{S}_{11}^{\lambda:\lambda+1} = \left[\mathbf{S}_{11}^{\lambda}\mathbf{S}_{11}^{\lambda+1}\right] + \left[\mathbf{S}_{11}^{\lambda}\mathbf{S}_{12}^{\lambda+1}\right]\left[\mathbf{I}_{5\times5} - \mathbf{S}_{21}^{\lambda}\mathbf{S}_{12}^{\lambda+1}\right]^{-1}\left[\mathbf{S}_{21}^{\lambda}\mathbf{S}_{11}^{\lambda+1}\right] \\ \mathbf{S}_{12}^{\lambda:\lambda+1} = \left[\mathbf{S}_{12}^{\lambda}\right] + \left[\mathbf{S}_{11}^{\lambda}\mathbf{S}_{12}^{\lambda+1}\right]\left[\mathbf{I}_{5\times5} - \mathbf{S}_{21}^{\lambda}\mathbf{S}_{12}^{\lambda+1}\right]^{-1}\left[\mathbf{S}_{22}^{\lambda}\right] \\ \mathbf{S}_{21}^{\lambda:\lambda+1} = \left[\mathbf{S}_{21}^{\lambda+1}\right] + \left[\mathbf{S}_{22}^{\lambda+1}\right]\left[\mathbf{I}_{5\times5} - \mathbf{S}_{21}^{\lambda}\mathbf{S}_{12}^{\lambda+1}\right]^{-1}\left[\mathbf{S}_{21}^{\lambda}\mathbf{S}_{11}^{\lambda+1}\right] \\ \mathbf{S}_{22}^{\lambda:\lambda+1} = \left[\mathbf{S}_{22}^{\lambda+1}\right]\left[\mathbf{I}_{5\times5} - \mathbf{S}_{21}^{\lambda}\mathbf{S}_{12}^{\lambda+1}\right]^{-1}\left[\mathbf{S}_{22}^{\lambda}\right], \end{cases} \tag{29}$$

as proposed in recent multilayered problems under surface loadings (Liu et al., 2018) and specific dislocated-multilayers with internal semicoherent interfaces (Vattré and Pan, 2019).

3.2. Extended boundary conditions for dislocation loops and dislocation arrays

In contrast with the perfectly bonded interfacial conditions, the introduction of finite dislocation loops L and infinitely long, straight and uniformly spaced parallel dislocation arrays A need specific boundary conditions, specified by

$$\begin{cases} t_K\left(x_1, x_2, z_{S+}, t\right) - t_K\left(x_1, x_2, z_{S-}, t\right) = 0 & \text{(30a)} \\ u_K\left(x_1, x_2, z_{S+}, t\right) - u_K\left(x_1, x_2, z_{S-}, t\right) = \mathrm{e}^{i\omega t}\,\hat{u}_K^p\left(x_1, x_2\right), & \text{(30b)} \end{cases}$$

where $z = z_{S-}$ and $z = z_{S+}$ denote the lower and upper sides of the dislocation surface $S = \{L, A\}$ at $z = z_S$, for which the traction field remains continuous. The prescribed time-independent displacement jump $\hat{u}_K^p\left(x_1, x_2\right)$ in the physical domain is

defined in eq. (30b) with respect to the corresponding constant Burgers vector b_K^S and is therefore expressed using analogous two-dimensional Fourier series, as follows

$$\hat{u}_K^p(x_1,x_2)=\begin{cases}\displaystyle\sum_{m=1}^{\infty}\sum_{n=1}^{\infty}\begin{bmatrix}\bar{b}_{mn}^x\cos(p_m x_1)\sin(q_n x_2)\\ \bar{b}_{mn}^y\sin(p_m x_1)\cos(q_n x_2)\\ \bar{b}_{mn}^z\sin(p_m x_1)\sin(q_n x_2)\\ \bar{b}_{mn}^\phi\sin(p_m x_1)\sin(q_n x_2)\\ \bar{b}_{mn}^\psi\sin(p_m x_1)\sin(q_n x_2)\end{bmatrix}\chi_L(x_1,x_2) \quad , \chi_L(x_1,x_2)=\begin{cases}1\ , \forall(x_1,x_2)\in L\\ 0\ , \text{otherwise}\end{cases} & \text{(31a)}\\ \displaystyle\sum_{m=1}^{\infty}\begin{bmatrix}\bar{b}_m^x\sin(w_m x_1)\\ \bar{b}_m^y\sin(w_m x_1)\\ \bar{b}_m^z\sin(w_m x_1)\\ \bar{b}_m^\phi\sin(w_m x_1)\\ \bar{b}_m^\psi\sin(w_m x_1)\end{bmatrix}, & \text{(31b)}\end{cases}$$

for dislocation loops and dislocation arrays, respectively. In eq. (31a), $\chi_S(x_1,x_2)$ is the two-dimensional indicator function for dislocation loops, while $w_m=2\pi m/\Lambda$ with $\Lambda=2L_x$ in eq. (31b) is the inter-dislocation spacing for one-dimensional dislocation network (Bonnet, 1996, Vattré, 2015, 2016). Without the time-dependent, sine and cosine proportional factors the expansion coefficients of the extended displacement discontinuity $[\![\bar{u}_K^{pS}]\!]$ for the dislocation loops and arrays are defined by

$$[\![\bar{\boldsymbol{u}}_K^{pS}]\!]=\begin{cases}\bar{\boldsymbol{b}}_{mn}^L=\left[\bar{b}_{mn}^x,\bar{b}_{mn}^y,\bar{b}_{mn}^z,\bar{b}_{mn}^\phi,\bar{b}_{mn}^\psi\right]^{\mathrm{t}}, & \text{for dislocation loops} & \text{(32a)}\\ \bar{\boldsymbol{b}}_m^A=-(\pi m)^{-1}\left[b_1^A,b_2^A,b_3^A,b_4^A,b_5^A\right]^{\mathrm{t}}, & \text{for dislocation arrays}, & \text{(32b)}\end{cases}$$

for which the latter physical MEE Burgers vector components b_K^A are crystallographically prescribed by constant components, related to either the bulk crystals for homophase interfaces (Hirth and Lothe, 1992, Sutton and Balluffi, 1995) or to the specific crystallographic characters for heterophase interfaces (Sutton and Balluffi, 1995, Vattré and Demkowicz, 2013). Especially, the components of the expansion coefficients in eqs. (32a) must also be determined with respect to the closed dislocation contours, such as the rectangular dislocation loops R of finite dimension $\ell_x\times\ell_y$ with center $[x_0=L_x/2,y_0=L_y/2,z_S]^{\mathrm{t}}$ as well as the elliptical dislocation loops E with major and minor semi-axes r_1 and r_2 centered about $[x_0,y_0,z_S]^{\mathrm{t}}$, which accounts for the particular case of circular dislocation loops C of radius $r=r_1=r_2$.

The first component $\bar{b}_{mn}^x$ of $\bar{\boldsymbol{b}}_{mn}^L$ in eq. (32a) is expressed by the finite integral transform technique, as follows

$$\bar{b}_{mn}^x=\frac{4}{L_xL_y}\int_0^{L_x}\int_0^{L_y}b_1^L\cos(p_m x_1)\sin(q_n x_2)\,\chi_L(x_1,x_2)\,dx_1\,dx_2\,, \tag{33}$$

which is reduced for a rectangular dislocation loop to

$$\bar{b}_{mn}^x=4\frac{b_1^R}{L_xL_y}\int_{L_x/2-\ell_x/2}^{L_x/2+\ell_x/2}\int_{L_y/2-\ell_y/2}^{L_y/2+\ell_y/2}\cos(p_m x_1)\sin(q_n x_2)\,dx_1\,dx_2\,, \tag{34}$$

where the integrand satisfies the Helmholtz equation, such that the expansion coefficients of the displacement components can be constructed in a specific system of vector functions, while the double integrals over rectangular regions lead to the following exact-closed form expression, as

$$\bar{b}_{mn}^x=\begin{cases}(-1)^{(n+1)/2+1}\dfrac{4\ell_x}{\pi nL_x}\sin\Big(\dfrac{n\pi\ell_y}{2L_y}\Big)b_1^R, & m=0\,,\ n=1,3,5,\dots\\ (-1)^{m/2}(-1)^{(n+1)/2+1}\dfrac{16}{\pi^2mn}\sin\Big(\dfrac{m\pi\ell_x}{2L_x}\Big)\sin\Big(\dfrac{n\pi\ell_y}{2L_y}\Big)b_1^R, & m=2,4,6,\dots\,,\ n=1,3,5,\dots\,,\end{cases} \tag{35}$$

with $L_x\gg\ell_x$ and $L_y\gg\ell_y$. The determination of $\bar{b}_{mn}^y$ is straightforwardly formulated by changing the physical Burgers vector component b_1^R with b_2^R, the expansion term m with n, the subscript x with y, and vice versa, while the remaining components $\bar{b}_{mn}^\eta$, with superscripts $\eta=\{z,\phi,\psi\}$ equivalent to subscripts $\eta=\{3,4,5\}$, are given by

$$\bar{b}_{mn}^\eta=(-1)^{(m+1)/2+1}(-1)^{(n+1)/2+1}\frac{16}{\pi^2mn}\sin\Big(\frac{m\pi\ell_x}{2L_x}\Big)\sin\Big(\frac{n\pi\ell_y}{2L_y}\Big)b_\eta^R, \quad m=1,3,5,\dots\,,\ n=1,3,5,\dots \tag{36}$$

which completes the expansion coefficients of the extended displacement discontinuity for dislocation loops in eq. (32a). On the other hand, eq. (33) for elliptical dislocation loops E becomes

$$\bar{b}_{mn}^x=4\frac{b_1^E}{L_xL_y}\int_0^{2\pi}\int_0^{r_\theta}\cos\big(p_m(r'\cos\theta+x_0)\big)\sin\big(q_n(r'\sin\theta+y_0)\big)\,r'dr'd\theta\,, \tag{37}$$

with $r_\theta=r_1r_2/\sqrt{(r_2\cos\theta)^2+(r_1\sin\theta)^2}$, which can be carried out with respect to r', as follows

$$\bar{b}_{mn}^x=2\frac{b_1^E}{L_xL_y}\int_0^{2\pi}\Big[a_3^{-2}\left(\sin(r_\theta a_3+a_4)-\sin a_4-r_\theta a_3\cos(r_\theta a_3+a_4)\right)-a_1^{-2}\left(\sin(r_\theta a_1+a_2)-\sin a_2-r_\theta a_1\cos(r_\theta a_1+a_2)\right)\Big]\,d\theta\,,$$
$$m=0,2,4,\dots\,,\ n=1,3,5,\dots\,,$$

(38)

where the Fourier mode-dependent parameters are given by

$$\begin{aligned} a_1 &= p_m \cos\theta - q_n \sin\theta\,, \quad & a_2 &= p_m x_0 - q_n y_0 \\ a_3 &= p_m \cos\theta + q_n \sin\theta\,, \quad & a_4 &= p_m x_0 + q_n y_0\,, \end{aligned} \tag{39}$$

with $m = 0, 2, 4, \ldots$, and, $n = 1, 3, 5, \ldots$ for both wave numbers p_m and q_n, respectively. Equation (38) leads therefore to a line-integral expression that is numerically computed for elliptical dislocation loops by use of standard Gauss quadrature rules. A similar line-integral expression is obtained for $\bar{b}^y_{mn}$, apart from m and n that run odd and even integers, respectively, while the remaining Fourier coefficients $\bar{b}^\eta_{mn}$ read

$$\begin{aligned} &\bar{b}^\eta_{mn} = 2\frac{b^C_\eta}{L_x L_y}\int_0^{2\pi}\left[a_1^{-2}\left(\cos\left(r_\theta a_1 + a_2\right) - \cos a_2 - r_\theta a_1 \sin\left(r_\theta a_1 + a_2\right)\right) - a_3^{-2}\left(\cos\left(r_\theta a_3 + a_4\right) - \cos a_4 - r_\theta a_3 \sin\left(r_\theta a_3 + a_4\right)\right)\right] d\theta\,, \\ &\quad m = 1, 3, 5, \ldots\,,\; n = 1, 3, 5, \ldots\,, \end{aligned} \tag{40}$$

with $\eta = \{z, \phi, \psi\} \equiv \{3, 4, 5\}$. Furthermore, the global propagation submatrices in eq. (29) from the bottom surface at $z = z_0 = 0$ to the top surface to $z = z_N = H$ can be partitioned to explicitly determine the displacement and traction solutions at any z-level including the conditions for the perfectly bonded interfaces as well as for the dislocation loops and arrays. The field solutions in the Fourier-transformed domain at z_f in layer λ can be obtained from eq. (28) by propagating first the transformed displacement and traction vectors from the bottom surface $z = 0$ to the lower side of the dislocation loop at $z = z_{S-}$, as follows

$$\begin{bmatrix} \bar{\boldsymbol{u}}\left(z = 0\right) \\ \bar{\boldsymbol{t}}\left(z = z_{S-}\right) \end{bmatrix} = \begin{bmatrix} \mathbf{S}_{11}^{1:\lambda} & \mathbf{S}_{12}^{1:\lambda} \\ \mathbf{S}_{21}^{1:\lambda} & \mathbf{S}_{22}^{1:\lambda} \end{bmatrix} \begin{bmatrix} \bar{\boldsymbol{u}}\left(z = z_{S-}\right) \\ \bar{\boldsymbol{t}}\left(z = 0\right) \end{bmatrix}, \tag{41}$$

and then, propagating the solution from the upper side at z_{S+} of the dislocation loop to the top surface $z = H$ to similarly obtain the subsequent relations

$$\begin{bmatrix} \bar{\boldsymbol{u}}\left(z = z_{S+}\right) = [\![\bar{\boldsymbol{u}}^{pS}_K]\!] + \bar{\boldsymbol{u}}\left(z = z_{S-}\right) \\ \bar{\boldsymbol{t}}\left(z = H\right) \end{bmatrix} = \begin{bmatrix} \mathbf{S}_{11}^{\lambda:N} & \mathbf{S}_{12}^{\lambda:N} \\ \mathbf{S}_{21}^{\lambda:N} & \mathbf{S}_{22}^{\lambda:N} \end{bmatrix} \begin{bmatrix} \bar{\boldsymbol{u}}\left(z = H\right) \\ \bar{\boldsymbol{t}}\left(z = z_{S+}\right) \end{bmatrix}, \tag{42}$$

for which the displacement jump condition in the reciprocal domain is incorporated. Both eqs. (41) and (42) can be conveniently recast into the following linear system, i.e.,

$$\begin{bmatrix} \mathbf{0}_{5\times5} & -\mathbf{I}_{5\times5} & \mathbf{S}_{11}^{\lambda:N} & \mathbf{S}_{12}^{\lambda:N} \\ \mathbf{0}_{5\times5} & \mathbf{0}_{5\times5} & \mathbf{S}_{21}^{\lambda:N} & \mathbf{S}_{22}^{\lambda:N} \\ -\mathbf{I}_{5\times5} & \mathbf{S}_{11}^{1:\lambda} & \mathbf{0}_{5\times5} & \mathbf{0}_{5\times5} \\ \mathbf{0}_{5\times5} & \mathbf{S}_{21}^{1:\lambda} & \mathbf{0}_{5\times5} & -\mathbf{I}_{5\times5} \end{bmatrix} \begin{bmatrix} \bar{\boldsymbol{u}}\left(z = 0\right) \\ \bar{\boldsymbol{u}}\left(z = z_{S-}\right) \\ \bar{\boldsymbol{u}}\left(z = H\right) \\ \bar{\boldsymbol{t}}\left(z = z_{S-}\right) \end{bmatrix} = \begin{bmatrix} [\![\bar{\boldsymbol{u}}^{pS}_K]\!] \\ \bar{\boldsymbol{t}}\left(z = H\right) = \mathbf{0}_{5\times1} \\ -\mathbf{S}_{12}^{1:\lambda}\,\bar{\boldsymbol{t}}\left(z = 0\right) = \mathbf{0}_{5\times1} \\ -\mathbf{S}_{22}^{1:\lambda}\,\bar{\boldsymbol{t}}\left(z = 0\right) = \mathbf{0}_{5\times1} \end{bmatrix}, \tag{43}$$

where the submatrices on the left-hand side are defined in eq. (29). The system in eq. (43) is therefore solved for each Fourier mode to determine the displacement fields at the three involved locations, i.e., $\bar{\boldsymbol{u}}\left(z = 0\right)$, $\bar{\boldsymbol{u}}\left(z_{S-}\right)$ and $\bar{\boldsymbol{u}}\left(z = H\right)$, as well as the internal traction, i.e., $\bar{\boldsymbol{t}}\left(z = z_S\right)$ at $z = z_{S-} = z_S$, with respect to the free-surface boundary conditions at the external surfaces, i.e., $\bar{\boldsymbol{t}}\left(z = 0\right) = \bar{\boldsymbol{t}}\left(z = H\right) = \mathbf{0}$, without loss of generality, as well as the prescribed dislocation-induced displacement jump $[\![\bar{\boldsymbol{u}}^{pS}_K]\!]$ from eq. (32) with eqs. (35) and (36) for rectangular dislocation loops, and eqs. (38) and (40) for elliptical loops. For any field point z_f in the layer λ_f below the location of the defect embedded in λ_S, thus with $0 < z_f < z_{S-}$, the recursive relations in eq. (28) are conveniently split as

$$\begin{cases} \begin{bmatrix} \bar{\boldsymbol{u}}\left(z = 0\right) \\ \bar{\boldsymbol{t}}\left(z = z_f\right) \end{bmatrix} = \begin{bmatrix} \mathbf{S}_{11}^{1:\lambda_f} & \mathbf{S}_{12}^{1:\lambda_f} \\ \mathbf{S}_{21}^{1:\lambda_f} & \mathbf{S}_{22}^{1:\lambda_f} \end{bmatrix} \begin{bmatrix} \bar{\boldsymbol{u}}\left(z = z_f\right) \\ \bar{\boldsymbol{t}}\left(z = 0\right) \end{bmatrix} \\ \begin{bmatrix} \bar{\boldsymbol{u}}\left(z = z_f\right) \\ \bar{\boldsymbol{t}}\left(z = z_S\right) \end{bmatrix} = \begin{bmatrix} \mathbf{S}_{11}^{\lambda_f:\lambda_S} & \mathbf{S}_{12}^{\lambda_f:\lambda_S} \\ \mathbf{S}_{21}^{\lambda_f:\lambda_S} & \mathbf{S}_{22}^{\lambda_f:\lambda_S} \end{bmatrix} \begin{bmatrix} \bar{\boldsymbol{u}}\left(z = z_{S-}\right) \\ \bar{\boldsymbol{t}}\left(z = z_f\right) \end{bmatrix}, \end{cases} \tag{44}$$

which can also be recast into the following linear system of equations, i.e.,

$$\begin{bmatrix} \mathbf{S}_{11}^{1:\lambda_f} & \mathbf{0}_{5\times5} & -\mathbf{I}_{5\times5} & \mathbf{0}_{5\times5} \\ \mathbf{S}_{21}^{1:\lambda_f} & -\mathbf{I}_{5\times5} & \mathbf{0}_{5\times5} & \mathbf{0}_{5\times5} \\ \mathbf{I}_{5\times5} & \mathbf{S}_{12}^{\lambda_f:\lambda_S} & \mathbf{0}_{5\times5} & \mathbf{0}_{5\times5} \\ \mathbf{0}_{5\times5} & \mathbf{S}_{22}^{\lambda_f:\lambda_S} & \mathbf{0}_{5\times5} & -\mathbf{I}_{5\times5} \end{bmatrix} \begin{bmatrix} \bar{\boldsymbol{u}}\left(z = z_f\right) \\ \bar{\boldsymbol{t}}\left(z = z_f\right) \\ \bar{\boldsymbol{u}}\left(z = 0\right) \\ \bar{\boldsymbol{t}}\left(z = z_S\right) \end{bmatrix} = - \begin{bmatrix} \mathbf{S}_{12}^{1:\lambda_f}\,\bar{\boldsymbol{t}}\left(z = 0\right) \\ \mathbf{S}_{22}^{1:\lambda_f}\,\bar{\boldsymbol{t}}\left(z = 0\right) \\ \mathbf{S}_{11}^{\lambda_f:\lambda_S}\,\bar{\boldsymbol{u}}\left(z = z_{S-}\right) \\ \mathbf{S}_{21}^{\lambda_f:\lambda_S}\,\bar{\boldsymbol{u}}\left(z = z_{S-}\right) \end{bmatrix}, \tag{45}$$

and be solved to determine the expansion coefficients of the extended displacement $\bar{\boldsymbol{u}}\left(z = z_f\right)$ and traction $\bar{\boldsymbol{t}}\left(z = z_f\right)$ fields, using the known displacement field solutions $\bar{\boldsymbol{u}}\left(z = z_{S-}\right)$ in the right-hand side, previously obtained from the resolution of

eq. (43). On the other hand, for any field solution at point z_f such that $z_{S+} < z_f < H$ in the layer λ_f, a similar system as eq. (45) leads to

$$\begin{bmatrix} \mathbf{S}_{11}^{\lambda_S:\lambda_f} & \mathbf{0}_{5\times5} & \mathbf{0}_{5\times5} & \mathbf{S}_{12}^{\lambda_S:\lambda_f} \\ \mathbf{S}_{21}^{\lambda_S:\lambda_f} & -\mathbf{I}_{5\times5} & \mathbf{0}_{5\times5} & \mathbf{S}_{22}^{\lambda_S:\lambda_f} \\ -\mathbf{I}_{5\times5} & \mathbf{S}_{12}^{\lambda_f:N} & \mathbf{S}_{11}^{\lambda_f:N} & \mathbf{0}_{5\times5} \\ \mathbf{0}_{5\times5} & \mathbf{S}_{22}^{\lambda_f:N} & \mathbf{S}_{21}^{\lambda_f:N} & \mathbf{0}_{5\times5} \end{bmatrix} \begin{bmatrix} \bar{\boldsymbol{u}}(z=z_f) \\ \bar{\boldsymbol{t}}(z=z_f) \\ \bar{\boldsymbol{u}}(z=H) \\ \bar{\boldsymbol{t}}(z=z_S) \end{bmatrix} = \begin{bmatrix} -[\![\bar{\boldsymbol{u}}_K^{pS}]\!] - \bar{\boldsymbol{u}}(z=z_{S-}) \\ \mathbf{0}_{5\times1} \\ \mathbf{0}_{5\times1} \\ \bar{\boldsymbol{t}}(z=H) = \mathbf{0}_{5\times1} \end{bmatrix}, \tag{46}$$

for which the displacement and traction expansion coefficients at $z = z_f$ are similarly solved in the Fourier-transformed domain with respect to $\bar{\boldsymbol{u}}(z = z_{S-})$ from eq. (43).

By virtue of the appropriate displacement jump $[\![\bar{\boldsymbol{u}}_K^{pS}]\!]$ in eq. (32) for the considered multilayered boundary-value problem, the extended dislocation-induced displacement and stress fields are finally obtained in the physical domain by introducing the time-dependent $\mathrm{e}^{i\omega t}$ as well as the sine and cosine terms in the solutions from eqs. (45) and (46), as formulated in eqs. (9) and (10), while completed with the in-plane stress components in eq. (23), respectively.

4. Example applications

Illustrative examples of the general and unified theory for nonlocal and time-harmonic dislocation loops and arrays in multilayered are presented in applications to nanoscale MEE multilayered structures. The present field solutions are first validated against existing results from three standard approaches limited to static and local elastic theory of both types of defects in homogeneous copper (Cu) and copper/niobium (Cu/Nb) bimaterials. The corresponding boundary-value problems as well as the materials properties are those of the cited references. The proposed framework is further applied at the nanoscale to analyze the specific effect of material anisotropy, MEE mismatch, multi-phase coupling, nonlocal parameter, vibration frequency, stacking sequences, on the dislocation-induced elastic, electric, and magnetic fields in homogeneous and heterogenous structures made of $CoFe_2O_4$ (magnetostrictive cobalt ferrite, CFO) and $BaTiO_3$ (piezoelectric barium titanate, BTO), for which the materials properties are listed in Ref. (Vattré and Pan, 2019). Without loss of generality, the x_1-, x_2- and x_3- axes are parallel to $[100]$, $[010]$ and $[001]$, respectively, while the dimensions of the following defects are characterized by $\ell_x = \ell_y = 2r = 10$ nm, unless stipulated otherwise.

4.1. Validation with existing analytical solutions

Static and local field solutions in terms of displacements and stresses produced by dislocation loops and arrays (solid lines) are compared with existing analytical results (symbols) for validation purposes. In these examples, the Burgers vectors for all dislocation configurations are defined along the vertical z-direction, without loss of generality. Figure (2a) shows the non-zero stress field components generated by a rectangular loop in a homogeneous and isotropic Cu material, while the existing results are determined from Hirth and Lothe (1992). Figure (2b) depicts the continuous components of the displacement field solutions on the heterophase interface of the anisotropic elastic Nb/Cu bimaterial induced by a circular loop within the middle of the lower Cu layer, which are compared with the results of Yuan et al. (2019). In comparison with the closed-form relations Chu and Pan (2014), Fig. (2c) presents the stress fields along the interface of the Cu/Nb bimaterial space, produced by a symmetric tilt grain boundary that is described as a network of uniformly spaced edge dislocations. For these two types of dislocations in the reduced application problems, namely the rectangular and circular shaped dislocation loops as well as the dislocation arrays in heterophase structures, the present field solutions are in very good agreement with the static and local analytical benchmarks, which partially validates the accuracy of the novel unified framework for subsequent prediction analysis in more general and advanced boundary-value problems in anisotropic MEE multilayers. In particular, Fig. (3) shows the strong effect of material anisotropy on static and local elastic stresses induced by a rectangular loop in a homogeneous Cu full-space (red lines based on cubic Cu), compared to the isotropic approximation of the elastic properties from Fig. (2a). The discrepancies caused by the isotropic elasticity, which are significant in the vicinity of the dislocation edges, have also important consequences on the driving forces for plastic activity as well as for the short-range interaction of the dislocations with further topological defects. Offering a crucial route to understanding the plasticity behind macroscropic phenomena, discrete dislocation dynamics cannot leave such effect of material anisotropy unexamined, which the most three-dimensional recent codes tend to incorporate to account for realistic calculations.

4.2. Glide components of the generalized Peach-Koehler forces on shear dislocation loops

The determination of the finite self-energy is of great importance to compute the non-singular driving forces acting on shear dislocation loops, without resorting to heuristic assumptions as the dislocation line tension approximation. For $l_E \neq 0$, the nonlocal core-spreading operation is also able to regularize the pure elastic as well as the MEE fields produced by discrete dislocation loops with explicit local curvature, which are, in turn, used to calculate the finite-valued and generalized Peach-Koehler force at any point $\boldsymbol{x}^{\partial L} = \left[x_1^{\partial L}, x_2^{\partial L}, z_S\right]^{\mathrm{t}}$ on the boundary ∂L of the dislocation loop. Without considering prescribed electric and magnetic charge densities on the dislocations, the Peach-Koehler force per unit length $f_k(\boldsymbol{x}^{\partial L})$ reads

$$f_k(\boldsymbol{x}^{\partial L}) = \varepsilon_{kil}\, b_j^L\, \xi_l(\boldsymbol{x}^{\partial L})\, \sigma_{ij}(\boldsymbol{x}^{\partial L}), \tag{47}$$

with lowercase subscripts, where ε_{kil} is the alternating tensor, and $\xi_l(\boldsymbol{x}^{\partial L})$ is the unit tangent vector of the dislocation at $\boldsymbol{x}^{\partial L}$, while the free-singularity self-stress $\sigma_{ij}(\boldsymbol{x}^{\partial L})$ is obtained by solving eqs. (45) and (46) with respect to the prescribed displacement jump in eq. (32) for the tractions, completed by the in-plane stress components from eq. (23). The glide component f^g of

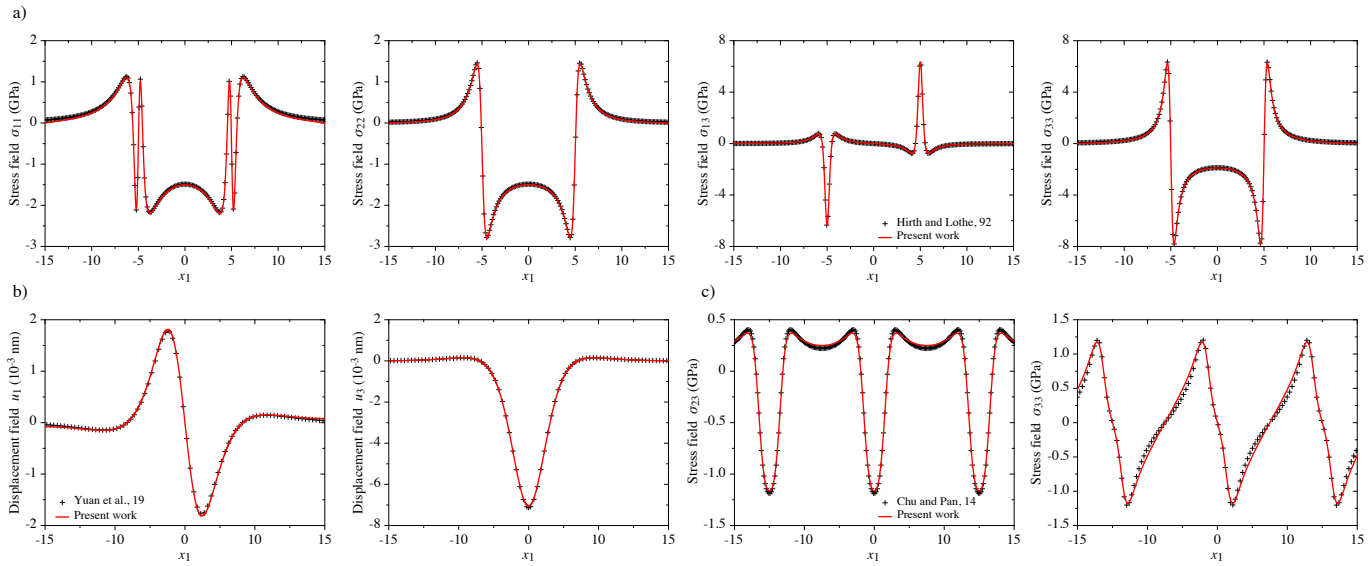

Figure 2: Comparison of static, local, and purely elastic field profiles obtained by the present theoretical solutions (solid lines) with analytics (symbols) for three different dislocated material configurations. For the three cases, the directions of the Burgers vectors are identical, and defined along $\boldsymbol{b} \parallel \boldsymbol{z} \parallel \boldsymbol{x}_3$. (a) A rectangular prismatic dislocation loop is located at z_L in the homogeneous and isotropic Cu material, and both stress components are displayed at $z = z_L + 2b$ along x_1, with $x_2 = L_y/2$. (b) A circular prismatic dislocation loop in the free-standing anisotropic Nb/Cu bimaterial is located in the center of the lower Cu plate at $z_L = h_{\text{Cu}}/2$, while the displacement components are plotted along the heterophase interface x_1-axis at $z = h_{\text{Cu}} = H/2$. (c) A low-angle tilt grain boundary located at $z = 8b$ in the Cu side from the heterophase interface of the semi-infinite anisotropic Cu/Nb bimaterial, for which the continuous stress components are displayed along the heterophase interface x_1-axis. The crosses in (a), (b) and (c) are obtained by the analytical solutions from Hirth and Lothe (1992), Yuan et al. (2019), and Chu and Pan (2014), respectively.

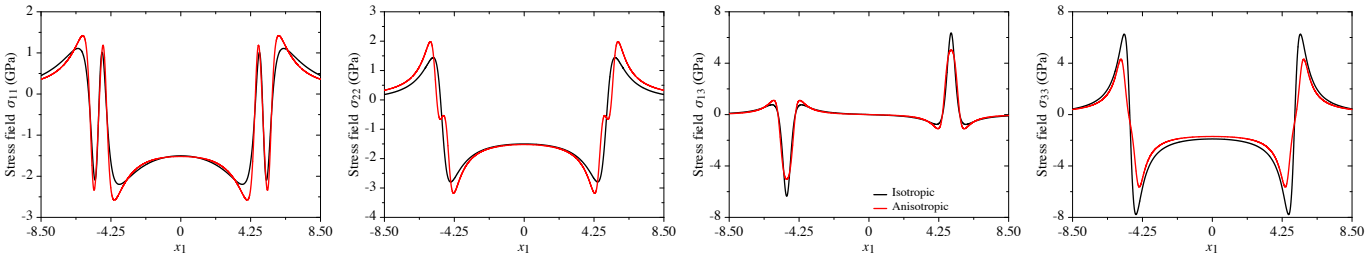

Figure 3: Static local isotropic (black lines) versus anisotropic (red lines) elastic stress field components produced by the specific configuration of rectangular and prismatic dislocation loop in Fig. (2a).

the dislocation force is also given by the projection of f_k onto $m_k(\boldsymbol{x}^{\partial L})$, where the latter is the unit and local outward-pointing direction vector in the plane, orthogonal to the loop. The magnitude of the Peach-Koehler forces is also signed, such that positive values describe the expansion of the dislocation loops, while the magnitude is reported as negative for dislocation shrinkage.

The effect of anisotropic elastic and time-harmonic field solutions on the Peach-Koehler forces along the elliptical shear dislocation loops is presented in Fig. (4). The uniform Burgers vector within the loops is oriented along the x_1-direction and the nonlocal parameter is set to $l_E = 0.15$ nm, while three elliptical shapes (i.e., with three different aspect ratios between r_1 and r_2) are considered in homogeneous copper. The plots are depicted as a function of the polar angle θ, for which $\theta \equiv 0$ mod 180° ($\theta \equiv 90^\circ$ mod 180°) corresponds to the part of dislocations with a pure edge (screw) character. Figure (4a) shows the variation of the static Peach-Koehler forces along the elliptical loops for the anisotropic (solid lines) and isotropic (dashed lines) elastic field solutions with respect to the three shapes, which are negative with θ for all dislocation configurations. Interestingly, the negative Peach-Koehler forces have maximum values in absolute amplitude at $\theta \equiv 90^\circ$ mod 180° for the isotropic calculations for circular and elliptical loops with $r_1 = r_2/2$, which on the other hand are minimum using the fully anisotropic elasticity theory. The schematics on the right-hand side of Fig. (4a) illustrate the distribution of the von Mises stress field as well as of the Peach-Koehler forces for the circular dislocation loop configuration embedded in anisotropic and isotropic elastic materials. The von Mises stress field and Peach-Koehler forces are more homogeneously distributed around the circular dislocation loop using the isotropic elastic approximation than for the anisotropic elastic case, for which the latter surprisingly exhibits the highest von Mises stress as well as the lowest resolved Peach-Koehler stress concentrations for the local screw characters. These deviations between isotropic and anisotropic elastic stress predictions are strongly expected to have a significant impact on the motion and dynamics of dislocation loops. In Fig. (4b), static self-stress field solutions using anisotropic elasticity for the three dislocation shapes in Fig. (4a) are compared to the time-harmonic dislocation cases with a fixed frequency $\omega = 3 \times 10^{12}$ rad/s. The main effect of the time-harmonic condition is to introduce an effective stress contribution to the Peach-Koehler forces for all three dislocation shapes, which roughly shifts the magnitude between the minimum and maximum values independently of θ, but has the serious consequence of leading the sign of the driving force to change locally, as illustrated by the grey shaded area. For illustration, the inset shows the change in sign over the large region of the elliptical dislocation loop with $r_1 = 2r_2$ near the screw characters.

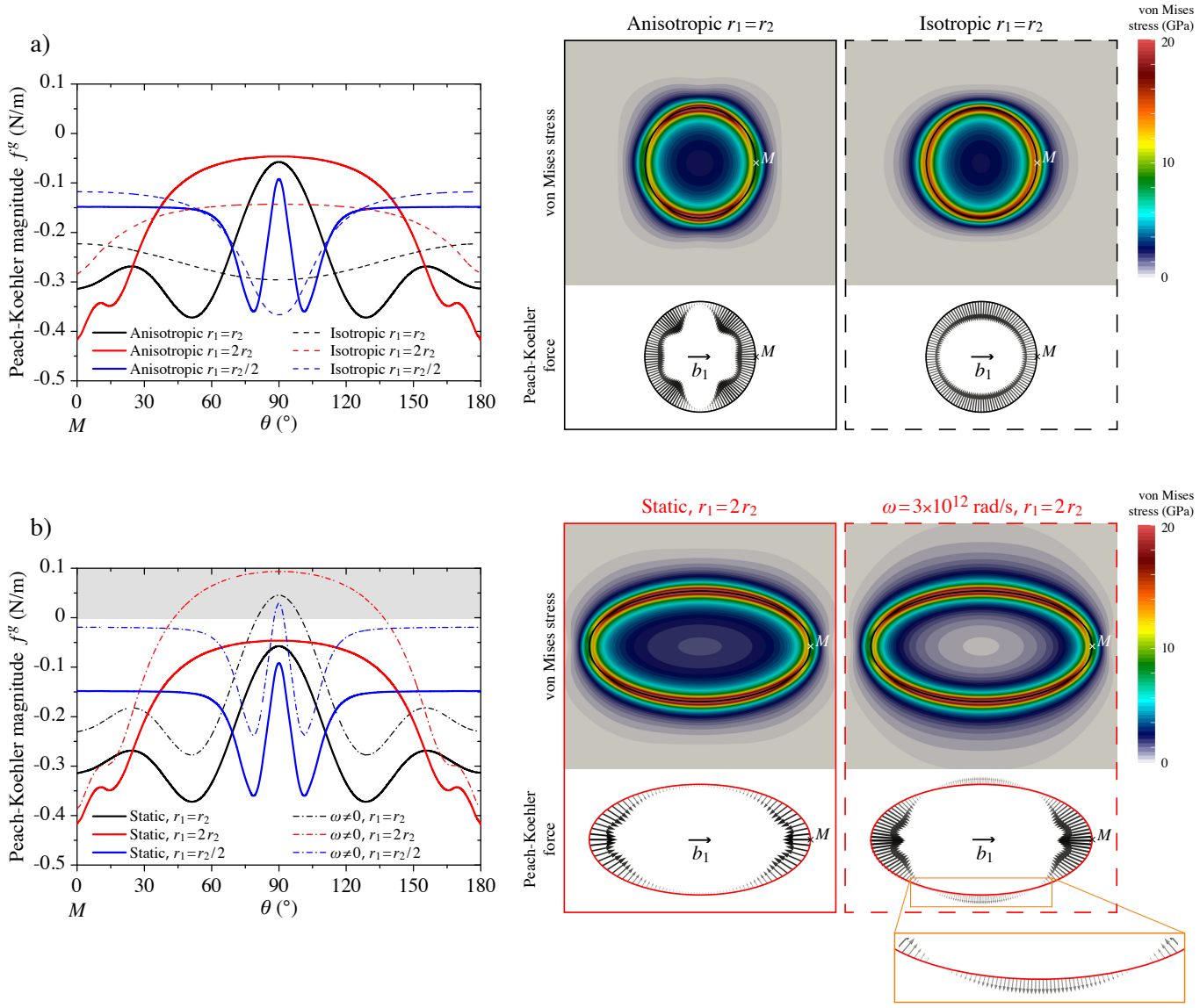

Figure 4: Effect of the (a) anisotropic (solid lines) versus isotropic (dashed lines) elasticity and of the (b) static (solid lines) versus time-harmonic (dashed lines) loading conditions on the non-singular magnitude of the glide component of the Peach-Koehler forces on circular, with $r_1 = r_2$ (black curves), as well as on two elliptical shear dislocation loops, with $r_1 = 2r_2$ (red curves) and $r_1 = r_2/2$ (blue curves), against the polar angle θ. The calculations are performed in copper, for which the Burgers vector b_1^L is oriented along the x_1-axis, as illustrated in the schematics, so that $\theta \equiv 0 \bmod 180^\circ$ corresponds to the points M on the dislocation fronts where the local character has a pure edge component. The nonlocal calculations are performed using $l_E = 0.15$ nm, and the magnitude of the Peach-Koehler forces in (b) are obtained by using the anisotropic elastic solutions and $\omega = 3 \times 10^{12}$ rad/s. The distribution of the von Mises stress field and the Peach-Koehler forces are displayed on the right-hand side for comparison between dissimilar configurations.

4.3. Nonlocal and time-harmonic dislocation-induced effects in MEE structures

Figure (5) shows the elastic displacements, electric and magnetic potentials, and stresses induced by a rectangular prismatic dislocation loop in a homogeneous and nonlocal MEE full-space, namely the BTO in Fig. (5a) and CFO in Fig. (5b) solids. Curves are plotted along the dislocation axis and two nonlocal parameter values are considered, for which the nonlocal field solutions are compared with the local MEE theory (dotted lines). As expected, the MEE field singularities in the local solids disappear due to the nonlocal effect, while a larger nonlocal parameter corresponds to a smoother field variation with a remarkable change in the magnitude and sign of the in-plane displacement u_1 as well as the transverse shear stress σ_{13}, especially in the CFO material. Interestingly, the nonlocal effect is mostly isolated in the vicinity of the dislocation cores, where singularity exists in the local solution, except for the electric and magnetic potentials where a broad nonlocal effect can be observed.

Figures (6a) and (b) illustrate the static and local MEE field components induced by a rectangular and prismatic dislocation loop embedded in the midway plane of two free-standing bimaterials made of BTO and CFO materials, namely the BTO/CFO and CFO/BTO bicrystals, respectively. The position of the dislocation loop is represented by the double-headed arrows, while the corresponding heterophase interfaces are located in the lower material at four different locations. The field solutions are displayed along a line in the z-direction that passes through the center of dislocations (as shown by the dotted vertical lines), parallel to Burgers vectors. As expected, the magnitude of the displacement jumps produced by the dislocation loops are in agreement with the prescribed Burgers vectors for both BTO/CFO and CFO/BTO bilayers, which approve the accuracy of numerical results. Due to the mismatch in MEE material properties between the two layers, strong discontinuities in terms of in-plane normal stress fields are observed at the cut surfaces, the magnitude of which is more pronounced the closer the interfaces are to the dislocation

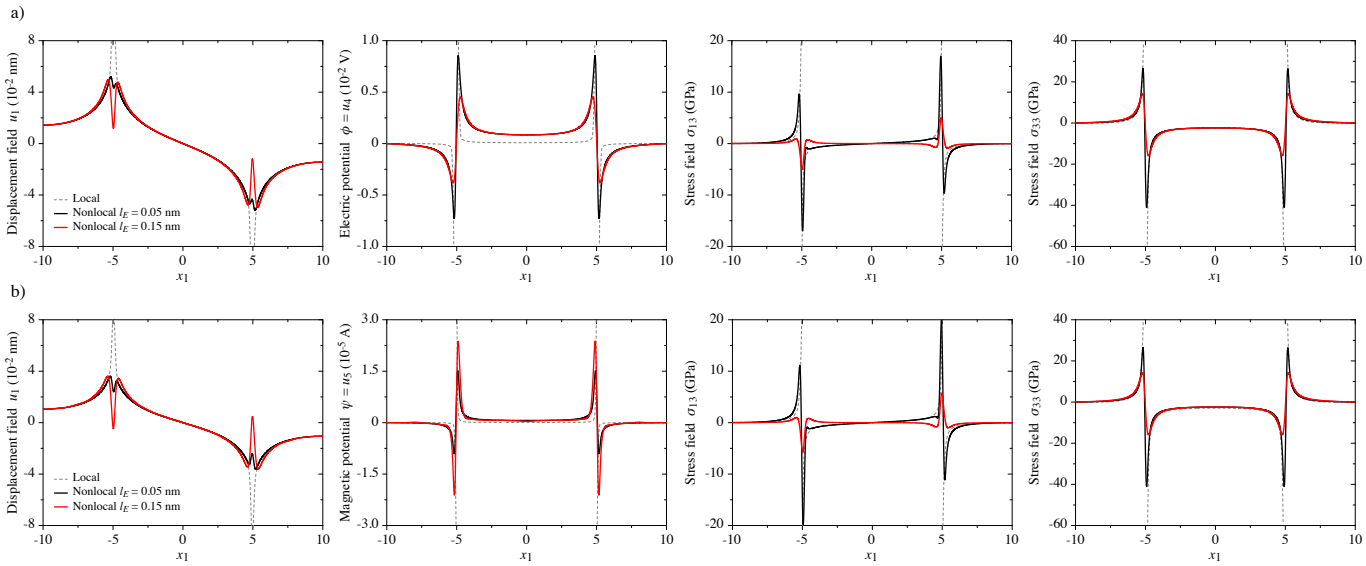

Figure 5: Influence of the nonlocal parameter on the static MEE field components produced by a rectangular prismatic dislocation loop embedded in homogeneous (a) BTO and (b) CFO solids. Curves are plotted along the dislocation axis.

loops. The stacking sequence has a major and surprising impact on the electric and magnetic potentials in sign, especially in BTO/CFO and CFO/BTO bimaterials, respectively. When the internal heterophase interface is farthest from the dislocation loop in the BTO/CFO (CFO/BTO) material system, the magnetic (electric) potential is almost zero, but becomes progressively more significant with decreasing the distance between the two different surface discontinuities. Such features could be valuable in understanding the role played by the change in sign of the electric field contribution on both properties of the propagating spin waves and the magnetoelectric effects for technological applications of magnetoelectric switching.

In addition to the calculations of the field solutions for rectangular and prismastic dislocation loop in Fig. (5a), Fig. (7) shows the static nonlocal MEE field components in a homogeneous BTO solid, induced by a low-angle tilt grain boundary. The symmetric boundary is also described by an infinitely long, straight and uniformly spaced parallel dislocations with the same edge characters for each intrinsic dislocation. Such polarization differs from the closed dislocation loop configuration, resulting in different displacement, stress and electric potential profiles along the tilt boundary. Dislocation arrays provide a locally weaker electric potential in magnitude than the dislocation loop by two orders of magnitude. As for the extrinsic defects, no singularities are obtained within the dislocation core regions due the nonlocal regularization term, in contrast with the local MEE calculations (dotted lines), so that the free-singularity stress fields lead to finite-valued driving forces for the intrinsic dislocations. For large values of the nonlocal parameter, camel bumps on the displacement profile appears, as in the case of the dislocation loop, while the spreading operation of the dislocation cores dramatically influences the component D_1 of the electric displacement, causing an abrupt change of sign and the appearance of a zero displacement plateau between two intrinsic dislocations.

Figures (8) shows the 2D contours of nonlocal MEE field solutions induced by a tilt grain boundary located at the center of the piezoelectric BTO materials and of the CFO/BTO/CFO trilayers, with $l_E = 0.05$ nm, as applied for the following calculations. The blue (red) color with negative (positive) values indicates the minimum (maximum) magnitude of the associated electric and magnetic variables, while the zeros are depicted in white. The location of the symmetric tilt grain boundary is represented by the double-headed arrows in the schematics for clarity. The maps of the electric and magnetic field solutions in the homogeneous BTO are significantly different from those in the CFO/BTO/CFO sandwich composite. The non-zero in-plane and normal electric displacement components are produced by the prescribed elastic displacement jumps at the tilt boundary in both systems. However, the electric displacement field is cut off in the two adjacent magnetostrictive materials of the trilayered structure, while the corresponding electric potential persists in both CFO plates, marked by a notable change in sign and high concentration near the internal heterophase interfaces. As expected, no magnetic properties are developed in the homogeneous BTO material, but the local elastic source in the central BTO plate of the trilayered structure is capable of producing coupling electric and magnetic fields, for which the latter is predominantly localized at the heterophase interfaces. This unique feature is also the consequence of the product composition in composites where, by stacking different layers with different couplings and thicknesses, remarkable coupling effects are experienced. A well-known characteristic is the magnetoelectric coupling coefficient that cannot be produced in a single BTO or CFO plates, but can be obtained in composite structures composed of both BTO and CFO materials.

Figures (9) shows the effect of the vibration frequencies $\omega = 0$ rad/s (static case), $\omega = 6 \times 10^{11}$ rad/s and $\omega = 2 \times 10^{12}$ rad/s on the nonlocal elastic fields, induced by the rectangular and prismatic dislocation configuration in homogeneous free-stranding (a) BTO and (b) CFO materials. In practice, the higher the frequency, the larger the difference between the maximum and minimum values of the signed displacement and stress magnitudes. In the BTO application case, the high excitation frequency results in a change in sign of the in-plane displacement field component, which could be particularly beneficial to engineers in developing self-powered switching designs for piezoelectric energy harvesting. The in-plane and normal stress field components are more meaningfully altered in magnitude at the center of the dislocation loops than at the dislocation cores with increasing vibration frequency amplitude. On the other hand, Fig. (10) shows spatially with more details the effect of frequency on the nonlocal MEE fields induced by a time-harmonic dislocation network of edge dislocations in a sandwich CFO/BTO/CFO trilayered structure.

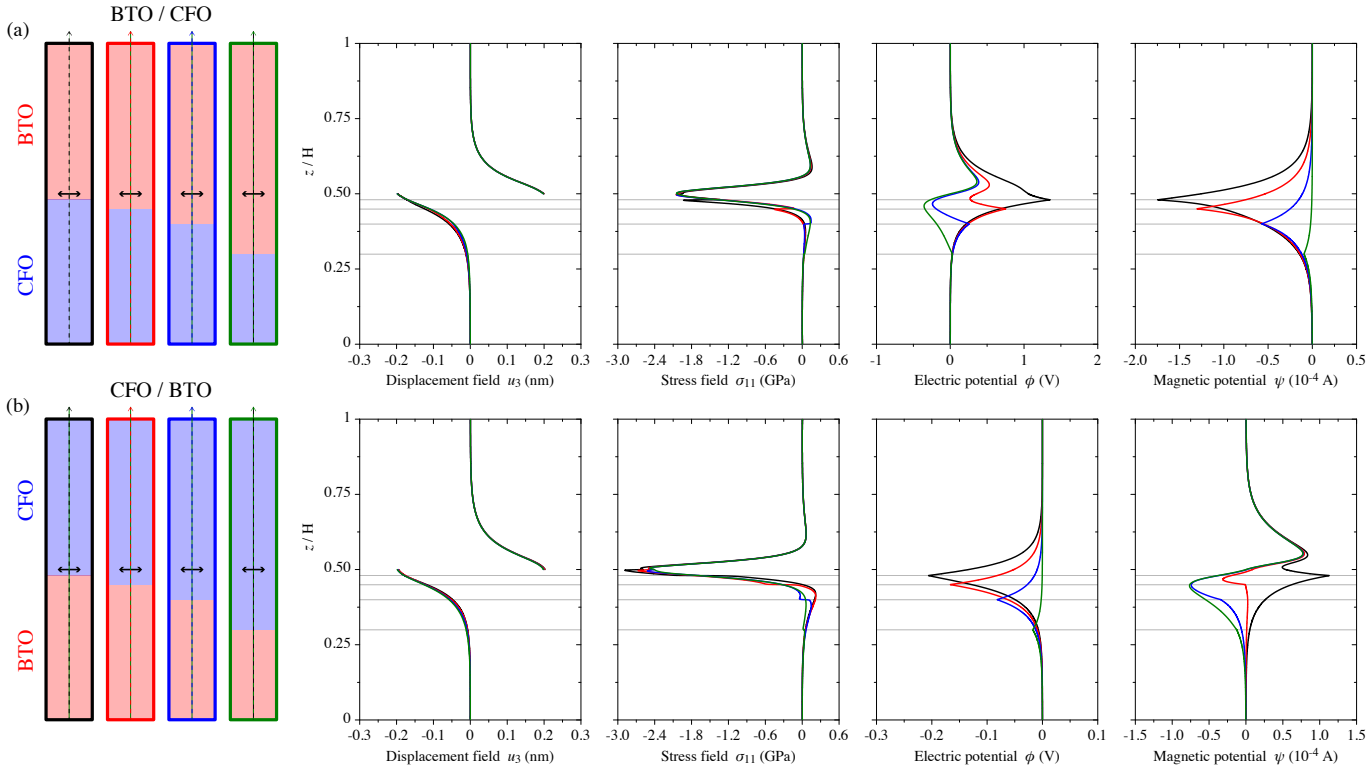

Figure 6: Influence of the MEE mismatch on the static MEE field components produced by a rectangular and prismatic dislocation loop embedded in heterogeneous (a) BTO/CFO and (b) CFO/BTO bilayers. The dislocation loop is located midway between the top and bottom free surfaces, as represented by the double-headed arrows, while the heterophase interfaces are situated at four different positions. Curves are plotted along the z-axis from the bottom and top free surfaces, as depicted by the vertical dotted lines.

The contour plots are presented for $\omega = 0$ rad/s versus $\omega = 18 \times 10^{11}$ rad/s. Again, it is obvious that the field response remarkably depends on the frequency in the material system, exhibiting significant difference in the MEE solutions. Especially, the elastic potential is mostly concentrated close to both internal CFO/BTO and BTO/CFO interfaces, while the normal magnetic induction is the largest at both upper and lower free surfaces. The elastic displacement and stress field components tend to spread over the entire trilayered structures with possible change in sign near to the free surfaces, while the equivalent von Mises stress leads to oscillating patterns for larger frequencies with a severe alternation of low and high values.

Finally, Fig. (11a) illustrates the complicated static and nonlocal magneto-electro-elastic interaction between a dislocation loop and periodically arranged edge dislocations of the tilt grain boundary in a BTO/CFO/BTO trilayered system, arbitrarily embedded in the piezomagnetic core plate. Without loss of generality, the Burgers vectors of the dislocation loop as well as the intrinsic dislocations are also identical and aligned with the normal vectors to the internal interfaces. Figure (11b) shows the isosurfaces of positive and negative magnetic induction values $B_z = \pm 0.3$ N/A.m induced by the prismatic dislocation loop, only. As excepted, the magnetic induction is confined in the CFO material, for which the negative in blue and positive values in red are found inside and outside the loop, respectively. Although the elastic discontinuity is located within the CFO layer, long-range electric displacements D_z are produced in the two adjacent BTO materials with asymmetric distributions due to the shifted position of the dislocation loop in the upper side of the core plate, as displayed in dark grey and yellow with magnitude $D_z = \pm 0.002$ C/m^2. The equivalent von Mises stress field generated by the superposition of both defects are depicted by the isosurface in Figs. (11c) and (d), where values of the total electric ($\phi = \pm 0.04$ V) and the total magnetic ($\psi = \pm 3 \times 10^{-5}$ A) potentials are mapped, respectively. For the specific configuration where the inter-dislocation distance is equal to the length of the dislocation loop, the stress state induced by the extrinsic defect has a wider range in the z-direction than the tilt grain boundary. Interestingly, the total electric potential is found localized at the internal BTO/CFO and CFO/BTO heterophase interfaces, with a specific electric polarization with respect to the direction of the elastic discontinuity jump, while the total magnetic potential is predominantly located within the vicinity of the edge dislocation cores of the symmetric tilt grain boundary.

5. Concluding remarks

A general and unified theory is developed to study the time-harmonic field solutions induced by dislocation loops and dislocation arrays in three-dimensional multiphase and multilayered nonlocal plates. The field expressions are derived in matrix form using Fourier series transforms, combined with the computationally powerful Stroh formalism and an unconditionally stable recursive technique to propagate the extended solutions among the different layers of the multilayered systems. For the first time, nonlocal and time-harmonic responses in orthotropic magneto-electro-elastic composites produced by extrinsic and intrinsic dislocations are considered in a fully unified framework. Although the present solutions encompass the reduced static and local elastic responses as special cases, also validated against closed-form solutions from the existing theoretical

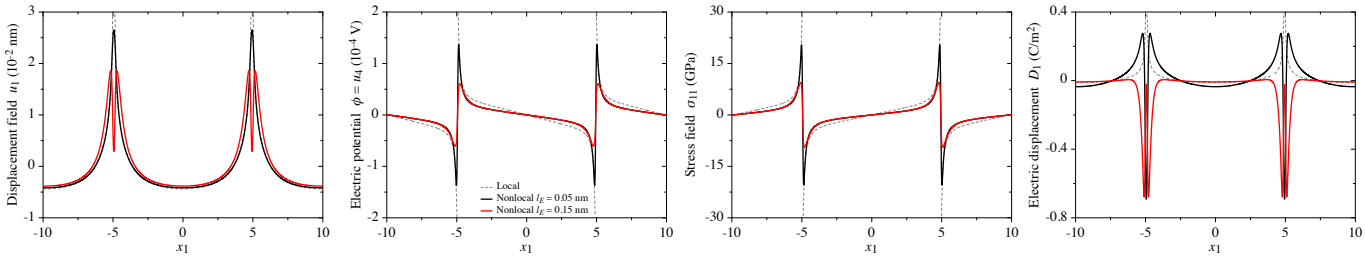

Figure 7: Influence of the nonlocal parameter on the static MEE field components produced by a tilt grain boundary in a homogeneous BTO material. The boundary is described by an infinitely long, straight and uniformly spaced parallel dislocations with edge characters. Curves are plotted along the tilt boundary for two nonlocal parameter values, while the local MEE calculations are shown for comparison.

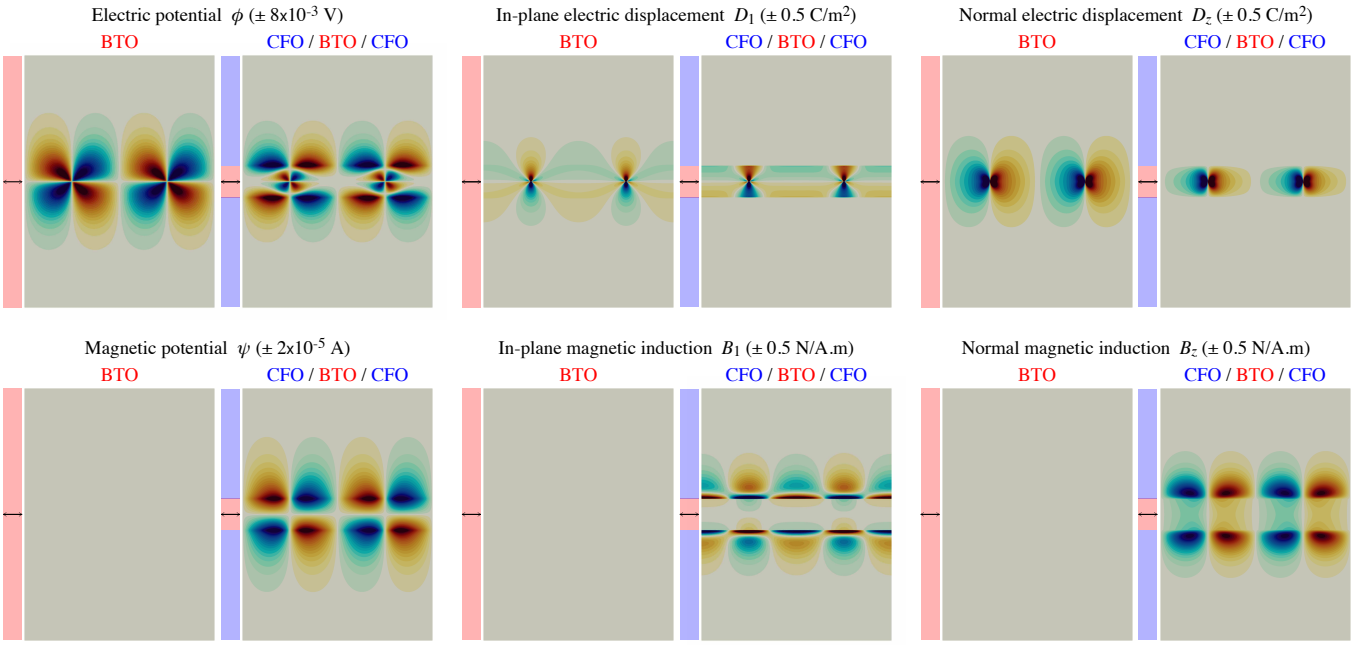

Figure 8: Contour plots of nonlocal electric and magnetic potential and displacement solutions for a tilt grain boundary located at the center of (a) a homogeneous BTO material and (b) a free-standing CFO/BTO/CFO trilayered structure. The blue (red) color with negative (positive) values represents the minimum (maximum) magnitude of the corresponding field components, while zeros are shown in white.

literature, the following important and interesting features observed on various boundary-value problems of dislocations in general magneto-electro-elastic layered systems are emphasized.

1) The effect of material anisotropy on the static and local elastic stresses induced by a rectangular loop in a homogeneous cubic Cu solid is significant in the vicinity of the dislocation edges. This feature is expected to have important consequences on the driving forces for dislocation nucleation, plastic deformation as well as for short-range interactions between extrinsic dislocations with other topological defects, in particular radiation-induced defects. Thus, to understand the plasticity behind the macroscopic phenomena using discrete dislocation dynamics, the effect of material anisotropy must be considered.

2) The stacking sequence has a major and surprising impact on the electric and magnetic fields when comparing BTO/CFO and CFO/BTO bilayers with a dislocation loop arbitrarily located in the bottom layers. The magnitude and especially the sign of the induced electric and magnetic fields are changed with respect to the distance of the dislocations from the internal heterophase interfaces. This result highlights the significant role played by the magneto-electro-elastic mismatch in investigating the interaction between dislocation loops and hetereophase interfaces. For example, the interesting change in sign of the electric field from the magneto-electro-elastic mismatch could be useful in designing the magneto-electric coupling for possible technological applications of reversible magneto-electric switching in three-dimensional multiferroic heterostructures.

3) As commonly reported, the singularities in the local magneto-electro-elastic field solutions are removed when the nonlocal effect is taken into account. A larger nonlocal parameter results in a smoother field variation with a remarkable change in the magnitude and sign of the in-plane displacement as well as the transverse shear stress states, especially in the CFO material. Furthermore, the nonlocal effect is mainly concentrated in the vicinity of the dislocation cores, for which a singularity occurs in the local solutions, except for the electric and magnetic potentials where a more widespread distributed influence of the nonlocal parameters is substantially observed.

4) In specific frequency regimes, the field solutions induced by time-harmonic dislocation loops and dislocation arrays lead to oscillatory responses. Specifically, a larger difference between the maximum and minimum values of the elastic field magnitudes corresponds to a higher frequency. However, in high-frequency BTO materials, a high excitation frequency results in a change of sign in the displacement field state, which could also be particularly useful to engineers in developing self-powered switching designs for piezoelectric energy harvesting.

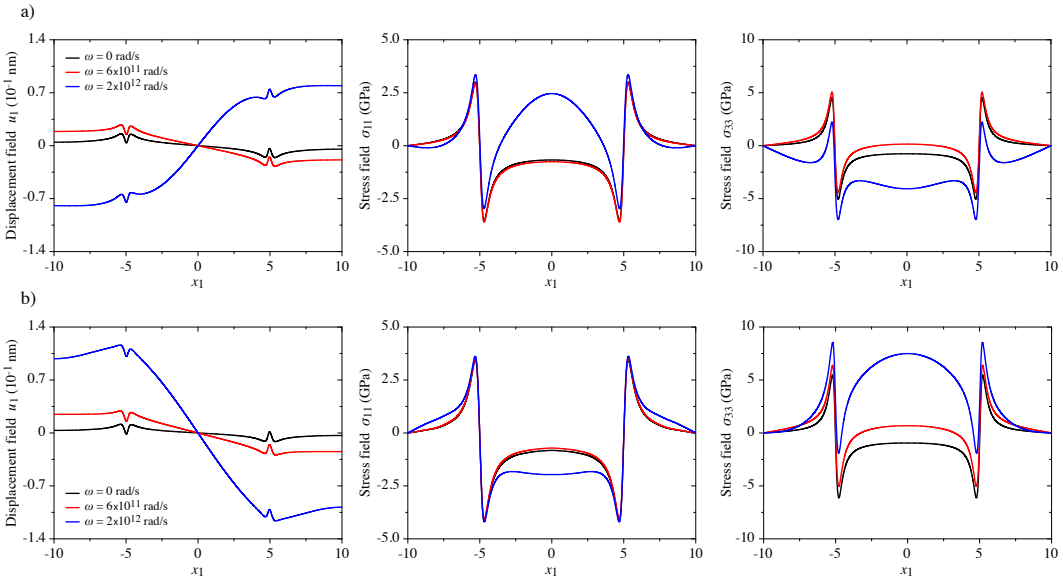

Figure 9: Effect of the frequencies on the nonlocal elastic field solutions produced by the rectangular and prismatic dislocation loop embedded in homogeneous free-stranding (a) BTO and (b) CFO materials. Curves are plotted along the dislocation axis.

5) Three-dimensional maps of the magneto-electro-elastic interaction between a dislocation loop and periodically arranged edge dislocations, arbitrarily embedded in the piezomagnetic core plate of a BTO/CFO/BTO trilayered structure, reveal that the total electric potential is preferentially localized at the internal heterophase interfaces, with a specific electric polarization, while the total magnetic potential is strongly located within the vicinity of the edge dislocation cores of the low-angle tilt grain boundary.

References

van Suchtelen, J., 1972. Product properties: a new application of composite materials. Phillips Research Reports, 27, 28-37.

van den Boomgaard, J., Terrell, D.R., Born, R.A.J., Giller, H.F.J.I., 1974. An in situ grown eutectic magnetoelectric composite material: Part 1. Composition and unidirectional solidifcation. Journal of Material Science, 9, 1705-1709.

van Run, A.M.J.G., Terrell, D.R., Scholing, J.H., 1974. An in situ grown eutectic magnetoelectric composite material: Part 2. Physical properties. Journal of Material Science, 9, 1710-1714.

Alshits, V.I., Darinskii, A.N., Lothe, J., 1992. On the existence of surface waves in half-anisotropic elastic media with piezoelectric and piezomagnetic properties. Wave Motion, 16, 265-283.

Harshe, G., Dougherty, J.P., Newnham, R.E., 1993. Theoretical modeling of multilayer magnetoelectric composites. International Journal of Applied Electromagnetics and Mechanics, 4, 145-159.

Chung, M.Y., Ting, T.C.T., 1995. The Green function for a piezoelectric piezomagnetic anisotropic elastic medium with an elliptic hole or rigid inclusion. Philosophical Magazine Letters, 72, 405-410.

Liu, J.X., Liu, X.L., Zhao, Y.B., 2001. Green's functions for anisotropic magnetoelectro-elastic solids with an elliptical cavity or a crack. International Journal of Engineering Science, 39, 1405-1418.

Pan, E., 2001. Exact solution for simply supported and multilayered magneto-electro-elastic plates. Journal of Applied Mechanics, 68, 608-618.

Pan, E., 2002. Three-dimensional Green's functions in anisotropic magneto-electro-elastic bimaterials. Zeitschrift für Angewandte Mathematik und Physik, 53, 815-838.

Wang, X., Shen, Y.-P., 2002. The general solution of three-dimensional problems in magnetoelectroelastic media. International Journal of Engineering Science, 40, 1069-1080.

Bichurin, M. I., Petrov, V. M., Srinivasan, G., 2003. Theory of low-frequency magnetoelectric coupling in magnetostrictive-piezoelectric bilayers. Physical Review B, 68, 054402.

Pan, E., Han, F., 2005. Exact solution for functionally graded and layered magneto-electro-elastic plates. International Journal of Engineering Science, 43, 321-339.

Challagulla, K.S., Georgiades, A.V., 2011. Micromechanical analysis of magneto-electro-thermo-elastic composite materials with applications to multilayered structures. International Journal of Engineering Science, 49, 85-104.

Zhang, D.P., Lei, Y.J., Shen, Z.B., 2017. Thermo-electro-mechanical vibration analysis of piezoelectric nanoplates resting on viscoelastic foundation with various boundary conditions. International Journal of Mechanical Sciences, 131, 1001-1015.

Ghobadi, A., Beni, Y.T., Golestanian, H., 2019. Size dependent thermo-electro-mechanical nonlinear bending analysis of flexoelectric nano-plate in the presence of magnetic field. International Journal of Mechanical Sciences, 152, 118-137.

Ngak, F.P.E., Ntamack, G.E., Azrar, L., 2019. Dynamic analysis of multilayered magnetoelectroelastic plates based on a pseudo-Stroh formalism and Lagrange polynomials. Journal of Intelligent Material Systems and Structures, 30, 939-962.

Ren, S., Meng, G., Cheng, F., Zhou, L., 2020. Transient responses of functionally graded magneto-electro-elastic structures with holes in thermal environment using stabilized node-based smoothed radial point interpolation method. International Journal of Mechanical Sciences, 185, 105870.

Bustamante, R., Shariff, M.H.B.M., Hossain, M., 2021. Mathematical formulations for elastic magneto-electrically coupled soft materials at finite strains: Time-independent processes. International Journal of Engineering Science, 159, 103429.

Tang, Y., Ma, Z-S., Ding, Q., Wang, T., 2021. Dynamic interaction between bi-directional functionally graded materials and magneto-electro-elastic fields: A nano-structure analysis. Composite Structures, 264, 113746.

Vinyas, M., 2021. Computational analysis of smart magneto-electro-elastic materials and structures: review and classification. Archives of Computational Methods in Engineering, 28, 1205-1248.

Yu, C., Kang, G., 2021. A multiscale magneto-thermo-mechanically coupled model for ultra-low-field induced magneto-electrocaloric effect in magnetostrictive-shape memory alloy composite system. International Journal of Engineering Science, 168, 103539.

Nagarajan, V., Jia, C.L., Kohlstedt, H., Waser, R., 2005. Misfit dislocations in nanoscale ferroelectric heterostructures. Applied Physics Letters, 86, 192910.

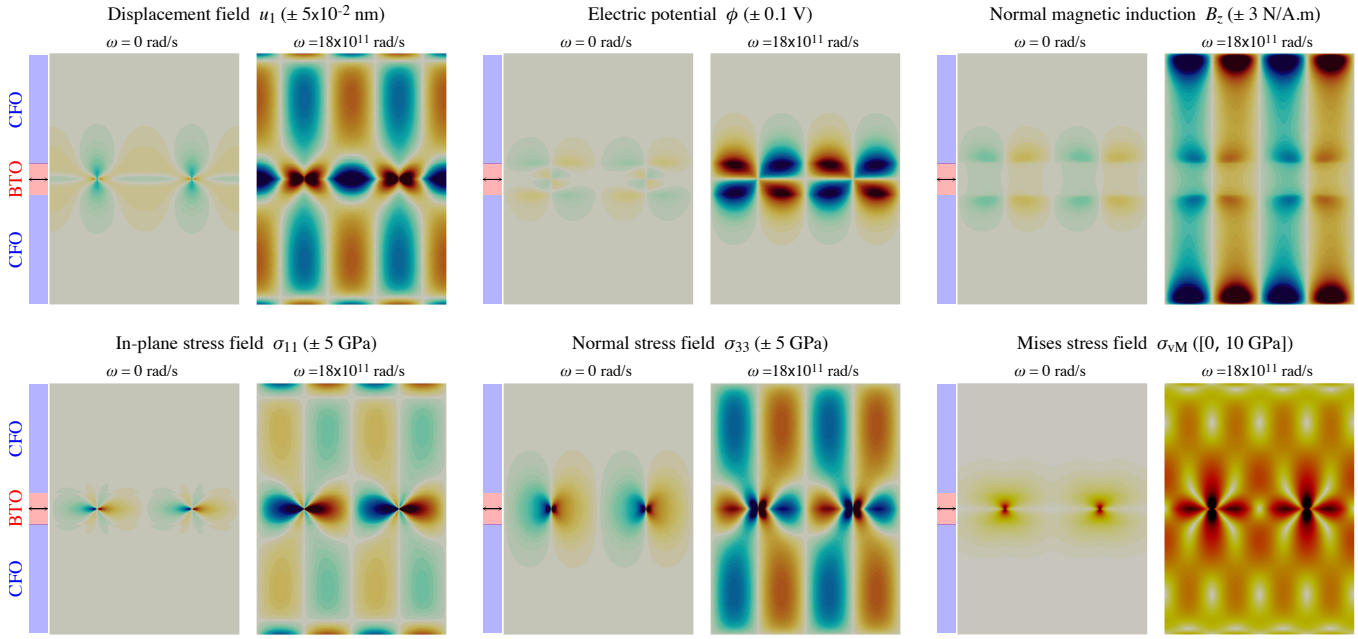

Figure 10: Effect of the frequencies on the nonlocal MEE field solutions induced by a time-harmonic tilt grain boundary of edge dislocations in a free-standing a CFO/BTO/CFO trilayered system. The blue (red) color with negative (positive) values represents the minimum (maximum) magnitude of the corresponding field components, while zeros are shown in white.

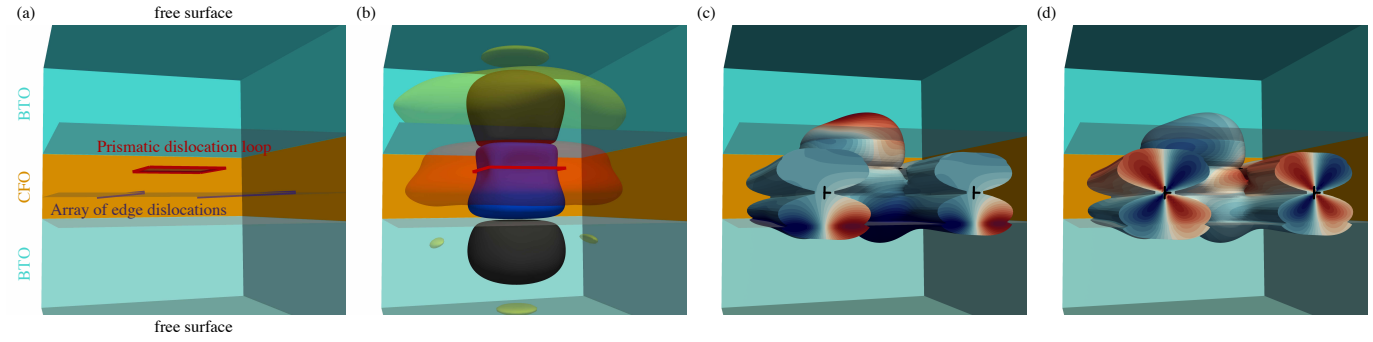

Figure 11: Static and nonlocal magneto-electro-elastic interaction between a rectangular prismatic dislocation loop and a dislocation array with edge characters in a BTO/CFO/BTO trilayered system. (a) Configuration where both defects are arbitrarily embedded in the central piezomagnetic CFO plate. (b) Isosurfaces of the normal electric displacement D_z, with magnitude $D_z = -0.002$ C/m^2 in dark grey, and $D_z = 0.002$ C/m^2 in yellow, as well as of the magnetic induction B_z, with $B_z = -0.3$ N/A.m in blue, and $B_z = 0.3$ N/A.m in red, induced by the prismatic dislocation loop, only. Isosurface of the von Mises equivalent stress value of $\sigma_{vM} = 1$ GPa, produced by the two types of dislocations, where (c) the total electric potential ($\phi = \pm 0.04$ V) and (d) the total magnetic potential ($\psi = \pm 3 \times 10^{-5}$ A) are displayed. For both potentials, the blue (red) color with negative (positive) values represents the minimum (maximum) magnitude of the corresponding field components, while zeros are shown in white.

Liu, J. X., Liu, X. L., Zhao, Y. B., 2001. Green's functions for anisotropic magnetoelectroelastic solids with an elliptical cavity or a crack. International Journal of Engineering Science, 39, 1405-1418.

Gao, C.-F., Kessler, H., Balke, H., 2003. Crack problems in magnetoelectroelastic solids. Part I: exact solution of a crack. International Journal of Engineering Science, 41, 969-981.

Wang, B.L., Mai, Y.-W., 2003. Crack tip field in piezoelectric/piezomagnetic media. European Journal of Mechanics - A/Solids, 22, 591-602.

Rao, B.N., Kuna, M., 2008. Interaction integrals for fracture analysis of functionally graded magnetoelectroelastic materials. International Journal of Fracture, 153,15-37.

Li, Y.D., Lee, K.Y., 2010. Effects of magneto-electric loadings and piezomagnetic/piezoelectric stiffening on multiferroic interface fracture. Engineering Fracture Mechanics, 77,856-866.

Wan, Y., Yue, Y., Zhong, Z., 2013. A mode III crack crossing the magnetoelectroelastic bimaterial interface under concentrated magnetoelectromechanical loads. International Journal of Solids and Structures, 49, 3008-3021.

Hu, K., Chen, Z., 2015. Mode-I crack in a magnetoelectroelastic layer sandwiched by two elastic half-planes. Engineering Fracture Mechanics, 134, 79-94.

Bagheri, R., Ayatollahi, M., Mousavi, S.M., 2015. Analysis of cracked piezoelectric layer with imperfect non-homogeneous orthotropic coating. International Journal of Mechanical Sciences, 93, 93-101.

Mousavi, S.M., 2015. Dislocation-based fracture analysis of functionally graded magnetoelectroelastic solids. Journal of Applied Mathematics and Mechanics, 95, 1501-1513.

Zhao, Y., Zhao, M.H., Pan, E., 2015. Displacement discontinuity analysis of a nonlinear interfacial crack in three-dimensional transversely isotropic magneto-electro-elastic bi-materials. Engineering Analysis with Boundary Elements, 61, 254-264.

Bagheri, R., Ayatollahi, M., Mousavi, S.M., 2017. Stress analysis of a functionally graded magneto-electro-elastic strip with multiple moving cracks. Mathematics and Mechanics of Solids, 22, 304-323.

Zhao, M., Zhang, Q., Li, X., Guo, Y., Fan, C., 2019. An iterative approach for analysis of cracks with exact boundary conditions in finite magnetoelectroelastic solids. Smart Materials and Structures, 28, 055025.

Nourazar, M., Ayatollahi, M., 2020. Mixed mode analysis of multiple cracks in magneto-electro-elastic plane. Theoretical and Applied Fracture Mechanics, 108,102672.

Wu, T. H., Li, X.Y., Tang, H.P., 2021. Three-dimensional fields in an infinite transversely isotropic magneto-electro-elastic space with multiple coplanar penny-

shaped cracks. International Journal of Engineering Science, 159, 103434.
Hsu, C.W., Hwu, C., 2022. Coupled stretching-bending boundary element analysis for unsymmetric magneto-electro-elastic laminates with multiple holes, cracks and inclusions. Engineering Analysis with Boundary Elements, 139, 137-151.
Nan, C.-W., Liu, G., Lin, Y., 2003. Influence of interfacial bonding on giant magnetoelectric response of multiferroic laminated composites of $Tb_{1-x}Dy_xFe_2$ and $PbZr_xTi_{1-x}O_3$. Applied Physics Letters, 83, 4366.
Wang, X., Pan, E., 2007. Magnetoelectric effects in multiferroic fibrous composite with imperfect interface. Physical Review B, 76, 214107.
Pan, E., Wang, X., Wang, R., 2009. Enhancement of magnetoelectric effect in multiferroic fibrous nanocomposites via size-dependent material properties. Applied Physics Letters, 95, 181904.
Huang, Y., Li, X.F., 2010. Shear waves guided by the imperfect interface of two magnetoelectric materials. Ultrasonics, 50, 750-757.
Espinosa-Almeyda, Y., López-Realpozo, J.C., Rodríguez-Ramos, R., Bravo-Castillero, J., Guinovart-Díaz, R., Camacho-Montes, H., Sabina, F.J., 2011. Effects of interface contacts on the magneto electro-elastic coupling for fiber reinforced composites. International Journal of Solids and Structures, 48, 1525-1533.
Kuo, H.-Y., 2013. Effective property of multiferroic fibrous composites with imperfect interfaces. Smart Materials and Structures, 22, 105005.
Wang, Y.Z., 2015. Influences of imperfect interface on effective magnetoelectric properties in multiferroic composites with elliptical fibers. Smart Materials and Structures, 24, 045021.
Espinosa-Almeyda, Y., Camacho-Montes, H., Rodríguez-Ramos, R., Guinovart-Díaz, R., López-Realpozo, J.C., Bravo-Castillero, J., Sabina, F.J., 2017. Influence of imperfect interface and fiber distribution on the antiplane effective magneto-electro-elastic properties for fiber reinforced composites. International Journal of Solids and Structures, 112, 155-168.
Kuo, H.-Y., Wu,T.-J., Pan, E., 2018. Multilayer multiferroic composites with imperfect interfaces. Smart Materials and Structures, 27, 07532
Jiang, J., Zhu, J., Chen, W., 2017. Dispersion curves of magneto-electro-elastic imperfect cylinders filled with fluid. Mathematics and Mechanics of Solids, 24, 195-211.
Kuo, H.-Y., Huang, C.S., Pan, E., 2019. Effect of imperfect interfaces on the field response of multilayered magneto-electro-elastic composites under surface loading. Smart Materials and Structures, 28, 115006.
Pang, Y., Feng, W., Liu, J., Zhang, C., 2019. SH wave propagation in a piezoelectric/piezomagnetic plate with an imperfect magnetoelectroelastic interface. Waves in Random and Complex Media, 29, 580-594.
Yang, Y., Li, W-F., 2019. Bending and free vibration of a circular magnetoelectroelastic plate with surface effects. International Journal of Mechanical Sciences, 157, 858-871.
Fang, Q.H., Liu, Y.W., Jiang, C.P., 2005. On the interaction between a generalized screw dislocation and circular-arc interfacial rigid lines in magnetoelectroelastic solids. International Journal of Engineering Science 43, 1011-1031.
Hao, R.J., Liu, J.X., 2006. Interaction of a screw dislocation with a semi-infinite interfacial crack in a magneto-electro-elastic bi-material. Mechanics Research Communications, 33, 415-424.
Zheng, J.L., Fang, Q.H., Liu, Y.W., 2007. A generalized screw dislocation interacting with interfacial cracks along a circular inhomogeneity in magnetoelectroelastic solids. Theoretical and Applied Fracture Mechanics, 47, 205-218.
Han, X., Pan, E., 2019. Fields produced by three-dimensional dislocation loops in anisotropic magneto-electro-elastic materials. Mechanics of Materials, 59, 110-125.
Chu, H., Wang, H., Zhao, Y., Pan, E., 2013. Dislocation and traction loads over an elliptical region in anisotropic magnetoelectroelastic bimaterials. Smart Materials and Structures, 22, 125020.
Moshtagh, E., Eskandari-Ghadi, M., Pan, E., 2019. Time-harmonic dislocations in a multilayered transversely isotropic magneto-electro-elastic half-space. Journal of Intelligent Material Systems and Structures, 30, 1932-1950.
Vattré, A., Pan, E., 2019. Semicoherent heterophase interfaces with core-spreading dislocation structures in magneto-electro-elastic multilayers under external surface loads. Journal of the Mechanics and Physics of Solids, 124, 929-956.
Yuan, J., Huang, Y., Chen, W., Pan, E., Kang G., 2019. Theory of dislocation loops in multilayered anisotropic solids with magneto-electro-elastic couplings. Journal of the Mechanics and Physics of Solids, 125, 440-471.
Bulatov, V.V., Cai, W., 2006. Computer simulations of dislocations. Oxford series on Materials Modelling. Oxford: Oxford University Press.
Kubin, L.P., 2013. Dislocations, mesoscale simulations and plastic flow. Oxford series on Materials Modelling. Oxford: Oxford University Press.
Cai, W., Nix, W.D., 2016. Imperfections in Crystalline Solids. Cambridge: Cambridge University Press.
Hirth, J.R., Lothe, L., 1992. Theory of dislocations. Second Edition. Florida: Krieger.
Sutton, A., Balluffi, R.,1995. Interfaces in Crystalline Materials. Oxford: Oxford University Press.
Vattré, A., Jourdan, T., Ding, H., Marinica, M.C., Demkowicz, M.J., 2016. Non-random walk diffusion enhances the sink strength of semicoherent interfaces. Nature communications, 7, 1-10.
Eshelby, J., Read, W., Shockley, W., 1953. Anisotropic elasticity with applications to dislocation theory. Acta Metallurgica, 1, 251-259.
Stroh, A.N., 1958. Dislocations and Cracks in Anisotropic Elasticity. Philosophical Magazine, 3, 625-646.
Stroh, A.N., 1962. Steady state problems in anisotropic elasticity. Journal of Mathematics and Physics, 41, 77-103.
Willis, J.R., 1970. Stress fields produced by dislocations in anisotropic media. Philosophical Magazine A, 21, 931-949.
Gavazza, S.D., Barnett, D.M., 1976. The self-force on a planar dislocation loop in an anisotropic linear-elastic medium. Journal of the Mechanics and Physics of Solids, 24, 171-185.
Ting, T.C.T, 1996. Anisotropic elasticity: theory and applications. New York: Oxford University Press.
Wang, C.-Y, 1996. The stress field of a dislocation loop in an anisotropic solid. Journal of the Mechanics and Physics of Solids, 44, 293-305.
Ohsawa, K., Yagi, M., Koizumi, H., Kuramoto, E., 2009. Stress function for dislocation loops in anisotropic crystals. Materials Science and Engineering, 3, 012027.
Lazar, M., Kirchner, H.O.K., 2013. Dislocation loops in anisotropic elasticity: displacement field, stress function tensor and interaction energy. Philosophical Magazine, 93, 174-185.
Pan, E., 2019. Green's functions for geophysics: a review. Reports on Progress in Physics, 82, 106801.
Chu, H.J., Pan, E., 2014. Elastic fields due to dislocation arrays in anisotropic bimaterials. International Journal of Solids and Structures, 51, 1954-1961.
Wu, W., Lv, C., Zhang, J., 2016. Interface traction stress of 3D dislocation loop in anisotropic bimaterial. Journal of the Mechanics and Physics of Solids, 87, 7-37.
Vattré, A., 2017a. Elastic strain relaxation in interfacial dislocation pattern: I. A parametric energy-based framework. Journal of the Mechanics and Physics of Solids, 105, 254-282.
Vattré, A., 2017b. Elastic strain relaxation in interfacial dislocation pattern: II. From long- to short-range interactions to local reactions. Journal of the Mechanics and Physics of Solids, 105, 283-305.
Vattré, A., Pan, E., 2018. Three-dimensional interaction and movements of various dislocations in anisotropic bicrystals with semicoherent interfaces. Journal of the Mechanics and Physics of Solids, 116, 185-216.
Ghoniem, N.M., Han, X., 2005. Dislocation motion in anisotropic multilayer materials. Philosophical Magazine, 85, 2809-2830.
Gao, Y., Larson, B.C., 2015. Displacement fields and self-energies of circular and polygonal dislocation loops in homogeneous and layered anisotropic solids. Journal of the Mechanics and Physics of Solids, 83, 104-128.
Lazar, M., Agiasofitou, E., 2011. Screw dislocation in nonlocal anisotropic elasticity. International Journal of Engineering Science 49, 1404-1414.
Lazar, M., Po, G., 2015. The non-singular Green tensor of gradient anisotropic elasticity of Helmholtz type. European Journal of Mechanics - A/Solids, 50, 152-162.
Lazar, M., Agiasofitou, E., Po, G., 2020. Three-dimensional nonlocal anisotropic elasticity: a generalized continuum theory of Ångström-mechanics. Acta Mechanica, 23, 743-781.

Ran, Y., Zhang, Y., Vishwanath, A., 2009. One-dimensional topologically protected modes in topological insulators with lattice dislocations. Nature Physics, 5, 298-303.
Tang, E., Fu, L., 2014. Strain-induced partially flat band, helical snake states and interface superconductivity in topological crystalline insulators. Nature Physics, 10, 964-969.
Sumiyoshi, H., Fujimoto, S., 2016. Torsional chiral magnetic effect in a Weyl semimetal with a topological defect. Physical Review Letters, 116, 166601.
Chernodub, M., Zubkov, M., 2017. Chiral anomaly in Dirac semimetals due to dislocations. Physical Review B, 95, 115410.
Hamasaki, H., Tokumoto, Y., Edagawa, K., 2017. Dislocation conduction in Bi-Sb topological insulators. Applied Physics Letters, 110, 092105.
Yang, Z., Tan, Y., Zu, J., 2017. A multi-impact frequency up-converted magnetostrictive transducer for harvesting energy from finger tapping. International Journal of Mechanical Sciences, 126, 235–241.
Chu, M.-W., Szafraniak, I., Scholz, R., Harnagea, C., Hesse, D., Alexe, M., Gösele, U., 2004. Impact of misfit dislocations on the polarization instability of epitaxial nanostructured ferroelectric perovskites. Nature Materials, 3, 87-90.
Jia, C.L., Mi, S.B., Urban, K., Vrejoiu, I., Alexe, M., Hesse, D., 2009. Effect of a Single Dislocation in a Heterostructure Layer on the Local Polarization of a Ferroelectric Layer. Physical Review Letters, 102, 117601.
Evans, D.M., Småbråten, D.R., Holstad, T.S., Vullum, P.E., Mosberg, A.B., Yan, Z., Bourret, E., van Helvoort, A.T.J., Selbach, S.M., Meier, D., 2021. Observation of Electric-Field-Induced Structural Dislocations in a Ferroelectric Oxide. Nano Letters, 21, 3386-3392.
Eringen, A.C., 2002. Nonlocal Continuum Field Theories. New-York: Springer.
Liu, H., Pan, E., Cai, Y., 2018. General surface loading over layered transversely isotropic pavements with imperfect interfaces. Advances in Engineering Software, 115, 268-282.
Thomson, W. T., 1950. Transmission of elastic waves through a stratified medium. Journal of Applied Physics, 21, 89-93.
Srinivas, S., Rao, A., 1970. Bending, vibration and buckling of simply supported thick orthotropic rectangular plates and laminates. International Journal of Solids and Structures, 6, 1463-1481.
Dobyns, A., 1981. Analysis of simply supported orthotropic plates subject to static and dynamic loads. AIAA Journal, 19, 642-650.
Haskell, N. A., 1953. The dispersion of surface waves on multilayered media. Bulletin of the Seismological Society of America, 43, 17-34.
Singh, S.J., 1970. Static deformation of a multilayered half-space by internal sources Journal of Geophysical Research, 75, 3257-3263.
Pan, E., 1989. Static response of a transversely isotropic and layered half-space to general surface loads. Physics of the Earth and Planetary Interiors, 54, 353-363.
Castaings, M., Hosten, B., 1993. Transfer matrix of multilayered absorbing and anisotropic media, Measurements and simulations of ultrasonic wave propagation through composite materials. Journal of the Acoustical Society of America, 94, 1488-1495.
Hosten, B., Castaings, M., 1993. Delta operator technique to improve the Thomson-Haskell-method stability for propagation in multilayered anisotropic absorbing plates. Journal of the Acoustical Society of America, 95, 1931-1941.
Nayfeh, A.H., 1991. The general problem of elastic wave propagation in multilayered anisotropic media. Journal of the Acoustical Society of America, 89, 1521-1531
Wang, L., Rokhlin, S.I., 2001. Stable reformulation of transfer matrix method for wave propagation in layered anisotropic media. Ultrasonics, 39, 413-424.
Rokhlin, S. I., Wang, L., 2002. Stable recursive algorithm for elastic wave propagation in layered anisotropic media: Stiffness matrix method. Journal of the Acoustical Society of America, 112, 822-834.
Tan, E.L., 2006. Hybrid compliance-stiffness matrix method for stable analysis of elastic wave propagation in multilayered anisotropic media. The Journal of the Acoustical Society of America, 119, 45-53.
Tan, E.L., 2007. Matrix Algorithms for Modeling Acoustic Waves in Piezoelectric Multilayers. IEEE Transactions on Ultrasonics, Ferroelectrics, and Frequency Control, 54, 2016-2023.
Tan, E.L., 2011. Recursive Asymptotic Hybrid Matrix Method for Acoustic Waves in Multilayered Piezoelectric Media. Open Journal of Acoustics, 1, 27-33.
Howard, S.M., Pao, Y.H., 1998. Analysis and experiments on stress waves in planar trusses. Journal of Engineering Mechanics - Asce, 124, 884-891.
Su, X.Y., Tian, J.Y., Pao, Y.H., 2002. Application of the reverberation-ray matrix to the propagation of elastic waves in a layered solid. International Journal of Solids and Structures, 39, 5447-5463.
Pao, Y.-H., Chen, W.Q., Su, X.Y., 2007. The reverberation-ray matrix and transfer matrix analyses of unidirectional wave motion. Wave Motion 44, 419-438.
Zhong, W.X., 2004. On precise integration method. Journal of Computational and Applied Mathematics, 163, 59-78
Gao, Q., Yao, W.A., Wu, F., Zhang, H.W., Lin, J.H., Zhong, W.X., Howson, W.P., Williams, F.W., 2103. An efficient algorithm for computing the dynamic responses of one-dimensional periodic structures and periodic structures with defects. Computational Mechanics, 52, 525-534.
Ai, Z.Y., Cheng, Y.C., 2014. Extended precise integration method for consolidation of transversely isotropic poroelastic layered media. Computers & Mathematics with Applications, 68, 1806-1818.
Zhou, J., Pan, E., Bevis, M., 2019. A point dislocation in a layered, transversely isotropic and self-gravitating Earth. Part I: analytical dislocation Love numbers. Geophysical Journal International, 217, 1681-1705.
Bonnet, R., 1996. Elasticity theory of straight dislocations in a multilayer. Physical Review B, 53, 10978.
Vattré, A., 2015. Mechanical interactions between semicoherent heterophase interfaces and free surfaces in crystalline bilayers. Acta Materialia, 93, 46-59.
Vattré, A., 2016. Elastic interactions between interface dislocations and internal stresses in finite-thickness nanolayered materials. Acta Materialia, 114, 184-197.
Vattré, A.J., Demkowicz, M.J., 2013. Determining the Burgers vectors and elastic strain energies of interface dislocation arrays using anisotropic elasticity theory. Acta Materialia, 14, 5172-5187.